STAR FORMATION IN EXTREME ENVIRONMENTS

RESOLVED STAR FORMATION IN LUMINOUS AND ULTRA-LUMINOUS INFRARED GALAXIES

By OSVALD KLIMI, BS (Math & Physics)

A Thesis Submitted to the School of Graduate Studies in Partial Fulfillment of the Requirements for the Degree Master of Science

McMaster University

MASTER OF SCIENCE (2024)

Hamilton, Ontario, Canada (Physics and Astronomy)

TITLE:	Resolved Star Formation in Luminous and Ultra-luminous Infrared Galaxies
AUTHOR:	Osvald Klimi BS (Math & Physics), McMaster University, Hamilton, Canada
SUPERVISOR:	Dr. Christine Wilson
NUMBER OF PAGES:	xv, 55

Abstract

This thesis investigates the gas content and star formation in a sample of 12 luminous and 4 ultra-luminous infrared galaxies (U/LIRGs). The primary aim is to analyze the relationship between those two properties to illuminate the physics driving star formation in these extreme environments. This is done through archival band 3 (84-116 GHz) Atacama Large Millimeter/submillimeter Array (ALMA) data. The tracers applied in this work are free-free radio continuum emission at 110 GHz for star formation rate surface density (Σ_{SFR}), CO (J=1-0) for bulk molecular gas surface density (Σ_{mol}), and CN (N=1-0) for dense molecular gas surface density (Σ_{dense}). Radio continuum images for each galaxy were created using Common Astronomy Software Applications (CASA) software package with the PHANGS-ALMA pipeline. Peaks in star formation efficiency for both bulk and dense gas align well with each other and with peaks in radio continuum emission. The galaxy NGC 3256 is highlighted as the main exception, where the locations of the peaks differ. The gas content displays a continuous distribution from spiral to U/LIRG data for both Σ_{mol} and Σ_{dense}, and the dense gas fraction is significantly higher in the U/LIRGs. A Kennicutt-Schmidt (KS) plot reveals a fairly shallow slope, nearly the same as what is seen in spirals, and a dense gas KS relation appears to have a tighter correlation than the bulk gas. This work finds gas depletion times as short as 10-100 Myr, compared to 0.3-3 Gyr for spiral data. This thesis also discusses potential sources of error such as using a single pair of conversion factors from molecular line intensities to gas surface density or contamination from an active galactic nucleus. These results from a substantial sample of 16 extreme galaxies offer valuable insights into the mechanisms driving star formation and potential for future research.

Për familjen time

Acknowledgements

I thanks my supervisor and committee for their comments and feedback that led to the best possible version of this work.

This thesis uses data from multiple ALMA projects. Thank you to Blake Ledger for proposing this master's thesis project and your role as a mentor, and sharing the following ALMA data:

ADS/JAO.ALMA#2012.1.00306.S,

ADS/JAO.ALMA#2012.1.00657.S,

ADS/JAO.ALMA#2013.1.00218.S,

ADS/JAO.ALMA#2013.1.00991.S,

ADS/JAO.ALMA#2013.1.01172.S,

ADS/JAO.ALMA#2015.1.00003.S,

ADS/JAO.ALMA#2015.1.00167.S,

ADS/JAO.ALMA#2015.1.00287.S,

ADS/JAO.ALMA#2015.1.01135.S,

ADS/JAO.ALMA#2015.1.01191.S,

ADS/JAO.ALMA#2016.1.00177.S,

ADS/JAO.ALMA#2016.1.00263.S,

ADS/JAO.ALMA#2017.1.00078.S,

ADS/JAO.ALMA#2018.1.00223.S,
ADS/JAO.ALMA#2018.1.01684.S, and
ADS/JAO.ALMA#2019.1.01664.S.

Thank you to Toshiki Saito for sharing data on NGC 1068 specifically, and for guidance on using the PHANGS-ALMA pipeline.

The spiral data used for comparison in this thesis is from Gallagher et al. 2018, which can be found online (Gallagher et al. 2019) with project codes: ADS/JAO.ALMA#2013.1.00634.S and ADS/JAO.ALMA#2011.0.00004.SV.

This thesis and other research like it is possible due to the archival data from ALMA. ALMA is a global partnership of the European Organisation for Astronomical Research in the Southern Hemisphere (ESO), the U.S. National Science Foundation (NSF) and the National Institutes of Natural Sciences (NINS) of Japan in cooperation with the Republic of Chile as the host. ALMA is funded by ESO on behalf of its Member States, by NSF alongside the National Research Council of Canada (NRC), the Ministry of Science and Technology (MOST) in Taiwan, NINS in cooperation with the Academia Sinica (AS) in Taiwan, and the Korea Astronomy and Space Science Institute (KASI). The facility is operated by ESO; by the National Radio Astronomy Observatory (NRAO)/Associated Universities, Inc. (AUI); and by the National Astronomical Observatory of Japan (NAOJ).

Thank you to my supervisor Dr. Christine Wilson for her support, the partial funding of my masters degree, and her depth of knowledge in teaching me both in the classroom and personally as my supervisor.

This research used the following software packages for python: ASTROPY (Collaboration 2013, Collaboration 2018, Collaboration 2022), CASA (McMullin et al. 2007), LinMix package (Meyers 2015) based on the work of Kelly (Kelly), MATPLOTLIB (Hunter 2007), NUMPY (Harris et al. 2020), SCIPY (Virtanen et al. 2020), and SPECTRAL-CUBE (Ginsburg et al. 2019).

Table of Contents

Abstract **iii**

Acknowledgements **vi**

Abbreviations **xiv**

1 Introduction and Literature Review **1**

1.1 Overview 1

1.2 Radio Astronomy 2

1.3 Star Formation and Gas Content 5

1.4 CN as a Tracer for Dense Gas 11

1.5 Goals 12

2 Data and Methods **14**

2.1 Sample Selection 14

2.2 Imaging the Radio Continuum Data 15

2.3 CO and CN maps 20

2.4 From Observables to Physical Quantities 21

3 Results and Discussions **24**
3.1 Efficiency Maps 25
3.2 Physics of Star Formation 27
3.3 Discussion 36

4 Conclusion and Future Work **39**

A SFE maps **43**

List of Figures

1.1 33 GHz radio emission vs other SFR tracers (Murphy et al. 2011). . . . 4

1.2 Total gas KS correlation (Kennicutt 1998). 6

1.3 Dense gas KS correlation (left) and bulk gas KS law (right) (Gao and Solomon 2004). 7

1.4 SFE_{dense} in 5 galactic disks vs bulk gas (Gallagher et al. 2018). 10

1.5 Dense gas KS relation for U/LIRGs and spirals (left) with corresponding depletion times (right) (García-Burillo et al. 2012). 11

1.6 KS law for 5 U/LIRGs (Wilson et al. 2019). 12

1.7 Constant I_{CN}/I_{HCN} ratio over many magnitudes of galactic properties such as SFR and bulk gas surface density (Wilson et al. 2023). 13

2.1 CARTA image of NGC 3256 with contour lines based on CO emission and apertures for radio intensity. 16

2.2a Radio continuum emission for the galaxies in this sample (1 of 2). . . 18

2.2b Radio continuum emission for the galaxies in this sample (2 of 2). . . 19

3.1 SFE maps for both bulk and dense gas for the galaxy NGC 6240. . . 26

3.2 SFE maps for both bulk and dense gas for the galaxy NGC 3256. . . 27

3.3 Comparing surface density of bulk and dense molecular gas. 28

3.4 Comparing dense gas fraction to bulk gas. 29

3.5 Kennicutt-Schmidt law for the sample of U/LIRGs. 30
3.6 Dense gas Kennicutt-Schmidt relation. 32
3.7 Star formation efficiency (inverse depletion time) against Σ_{mol}. 33
3.8 Star formation efficiency (inverse depletion time) of dense gas against Σ_{dense}. 34
3.9 Star formation efficiency (inverse depletion time) of dense gas against f_{dense}. 35
A.1 SFE maps for ARP 220. 43
A.2 SFE maps for ESO 320. 44
A.3 SFE maps for IRAS 13120. 44
A.4 SFE maps for IRAS f05189. 45
A.5 SFE maps for IRAS f10565. 45
A.6 SFE maps for IRAS f18293. 46
A.7 SFE maps for NGC 1068. 46
A.8 SFE maps for NGC 1365. 47
A.9 SFE maps for NGC 1614. 47
A.10 SFE maps for NGC 2623. 48
A.11 SFE maps for NGC 4418. 48
A.12 SFE maps for NGC 7469. 49

List of Tables

2.1 List of galaxies studied in this thesis. 15

Abbreviations

AGN	Active galactice nucleus
ALMA	Atacama Large Millimeter/submillimeter Array
CARTA	Cube Analysis and Rendering Tool for Astronomy
CASA	Common Astronomy Software Applications
CN	Cyanide
CO	Carbon monoxide
EMPIRE	EMIR Multiline Probe of the ISM Regulating Galaxy Evolution
GMC	Giant molecular cloud
GOALS	Great Observatories All-sky LIRG Survey
HCN	Hydrogen cyanide
HERUS	Herschel Ultra Luminous Infrared Galaxy Survey
IMF	Initial mass function
IR	Infrared

IRAM	Institut de radioastronomie millimétrique
ISM	Interstellar medium
KS	Kennicutt-Schmidt
LIRG	Luminous infrared galaxy
NAOJ	National Astronomical Observaotry of Japan
PHANGS	Physics at High Angular resolution in Nearby GalaxieS
SFR	Star formation rate
SFE	Star formation efficiency
ULIRG	Ultra-luminous infrared galaxy
UV	Ultraviolet

Chapter 1

Introduction and Literature Review

1.1 Overview

Star formation is a multi-faceted process occurring in many galaxies in which clouds condense under gravity and collapse into structures such as filaments and clumps, eventually building pre-stellar cores. Cold gas, particularly molecular hydrogen, serves as the raw material for forming new stars (Kennicutt and Evans 2012), with denser regions of this gas eventually collapsing under their own gravity to initiate nuclear fusion. Galaxy mergers play a significant role in triggering enhanced star formation rates (SFR; Sanders and Mirabel 1996). When galaxies collide or interact, their cold gas reservoirs can be compressed and destabilized, leading to the rapid formation of stars, often referred to as starburst events. These mergers can also boost star formation efficiency (SFE; Wilson et al. 2019), which is the rate of star formation per unit of gas, by driving gas into galactic centres where it can more easily collapse into stars. There are many ways to study star formation, such as by analyzing individual stellar populations or even single pre-stellar cores. In this thesis, I focus on the gas content on a scale of about 500pc, which can contain a few molecular clouds, and how that gas affects SFR.

1.2 Radio Astronomy

The star formation rate is a parameter which is central for many galactic studies, as it directly influences the growth, evolution, and observable properties of galaxies. In attempting to measure signals related to SFR, obscuration of the source due to dust is a common source of error observers consider and attempt to circumvent. Some tracers such as ultraviolet (UV) and Hα are quite susceptible to dust extinction, which is very common in mergers (Howell et al. 2010, Buat et al. 2010, Murphy et al. 2011). On the other hand, interpreting infrared (IR) emission as a SFR tracer has its own complications as it is produced as secondary emission from the very dust that obscures shorter wavelengths. Thus, it depends on the properties of the dust, and in addition some IR emission is contributed by older stars that have not recently formed (Murphy et al. 2011, Helou 1986, Persson and Helou 1987, Hirashita et al. 2003, Bendo et al. 2010, Li et al. 2010).

Radio wavelengths serve as a powerful and effective tool in the measurement of current star formation, providing a valuable alternative tracer. The benefit to high frequency (33 GHz in Murphy et al. 2011) thermal (free-free) radio emission is that it is not as susceptible to extinction from dust and the radio photons being emitted are related to newly formed massive stars (Murphy et al. 2011) Radio frequencies also allow for higher angular resolution. Murphy et al. (2011) analyze many regions in the nearby galaxy NGC 6946 and compare thermal radio emission between 24-40 GHz to multiple star formation tracers such as IR and 24μm emission, which are not affected by dust extinction, and combinations such as Hα + 24μm and UV + IR measurements, which correct for dust extinction by combining two wavelengths. Murphy et al. (2011) found that global measurements between 10 and 90 GHz do not have excess dust emission, and few individual regions contained such emission at all. The conclusion reached is that this radio emission (10-90 GHz) is dominated by free-free emission occurring in ionized gas. This ionized gas is a result of feedback from young massive stars (massive stars are short-lived), thus making radio emission between 10 to 90 GHz a viable SFR tracer.

Murphy et al. (2011) describe the prescription utilized to estimate star formation rate from radio emission. They desired to directly compare their star formation tracer to others and so used Starburst99 model prescriptions (Leitherer et al. 1999), a set of predictions for properties of galaxies with active star formation. They used a Kroupa IMF (initial mass function; Kroupa 1999) with a slope of -1.3 between $0.1 - 0.5M_{\odot}$ and -2.3 between $0.5 - 100M_{\odot}$. Additionally, they assume the 33 GHz radio emission is most accurate among the various tracers they compare as free-free emission produces 87% of the 33 GHz frequency (Murphy et al. 2011). Conversely, tracers that rely on dust emission overestimate the SFR, and non-thermal radio continuum underestimates SFR in non-nuclear regions of the galaxy (Murphy et al., 2011).

Figure 1.1 displays comparisons of observational SFR data - tracers such as IR and 1.4 GHz - against SFR traced by 33 GHz free-free emission. There are three prescriptions for the 33 GHz SFR: thermal (T), non-thermal (NT), and total. Murphy et al. (2011) find good agreement between the various diagnostic methods and 33

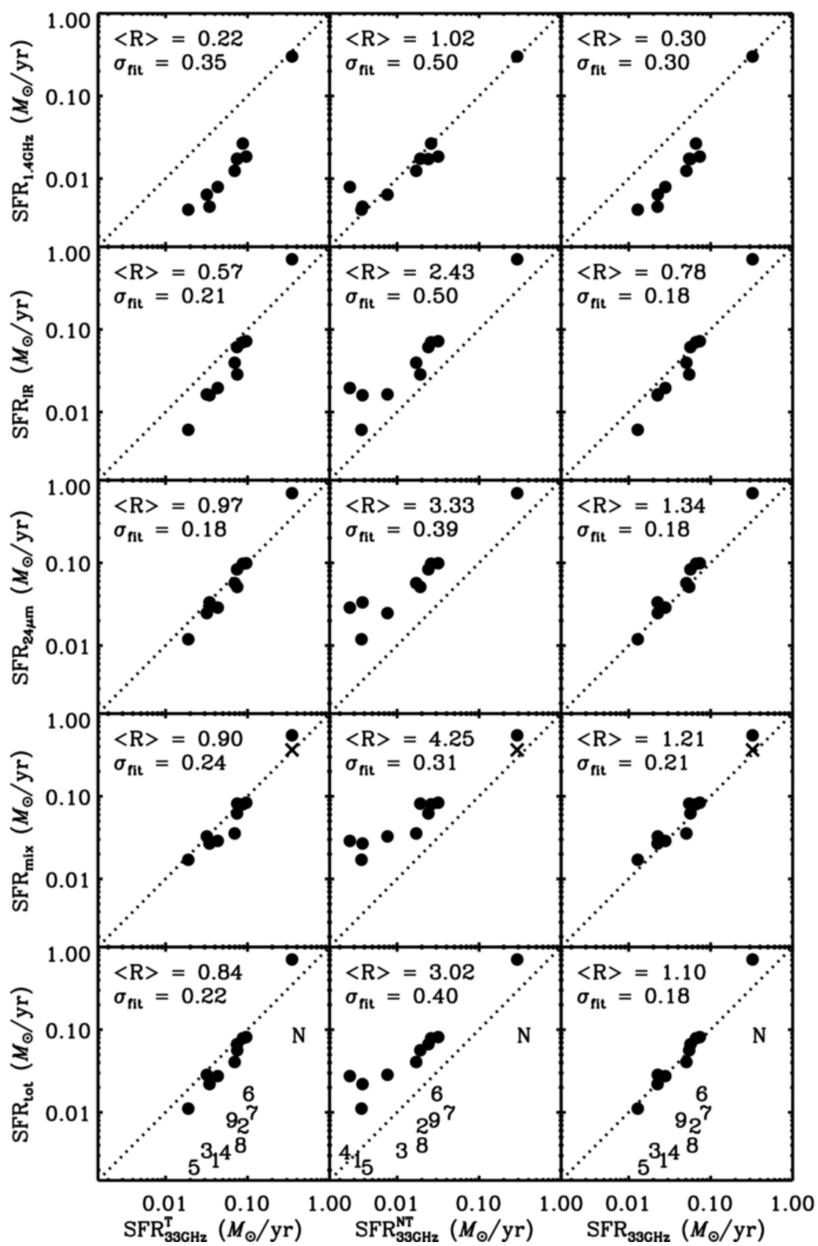

Figure 1.1: An array of comparisons between extinction independent tracers against the SFR from 33 GHz free-free emission tracer, the non-thermal radio emission, and total 33 GHz emission (Murphy et al., 2011). The rows are in order: 1.4 GHz, IR, 24 μm, Hα+ 24μm, UV+IR. The dotted lines are one-to-one relationships.

GHz radio continuum, though non-thermal 33 GHz emission appears slightly brighter compared to many other tracers (Murphy et al., 2011). The relevant equation I use in this thesis is equation (11) in their work (equation 2.4.2 in this thesis), which assumes 100% thermal emission to convert the radio luminosity to the total star formation. Further details about how I apply this equation to my data are elaborated in Chapter 2. This equation was also adapted for use in Wilson et al. (2019), which will be covered in more detail in Section 1.3.

1.3 Star Formation and Gas Content

Analysing physical properties of the interstellar medium (ISM) within a galaxy in addition to its SFR is critical in understanding the drivers causing star formation. To that end, many have applied star formation laws in order to characterise the relationship among gas and SFR, such as Schmidt (1959) and (Kennicutt 1989). Schmidt proposed a general star formation law which Kennicutt would characterise simply as

$$\Sigma_{SFR} = A\Sigma_{gas}^{N} \tag{1.3.1}$$

where Σ_{SFR} and Σ_{gas} are the SFR and gas surface densities, respectively, N was calibrated around 1.4 at the time of Kennicutt (1998) and A is a star formation efficiency. Kennicutt (1998) examined global data from 61 spiral galaxies and 36 luminous infrared galaxies (LIRGs) and reproduced a consistent power-law across multiple orders of magnitude in gas density and star formation.

Figure 1.2 (Figure 6 in Kennicutt, 1998) highlights a single least-squares fit with $N = 1.40$ for their entire sample of galaxies including normal spirals (black circles),

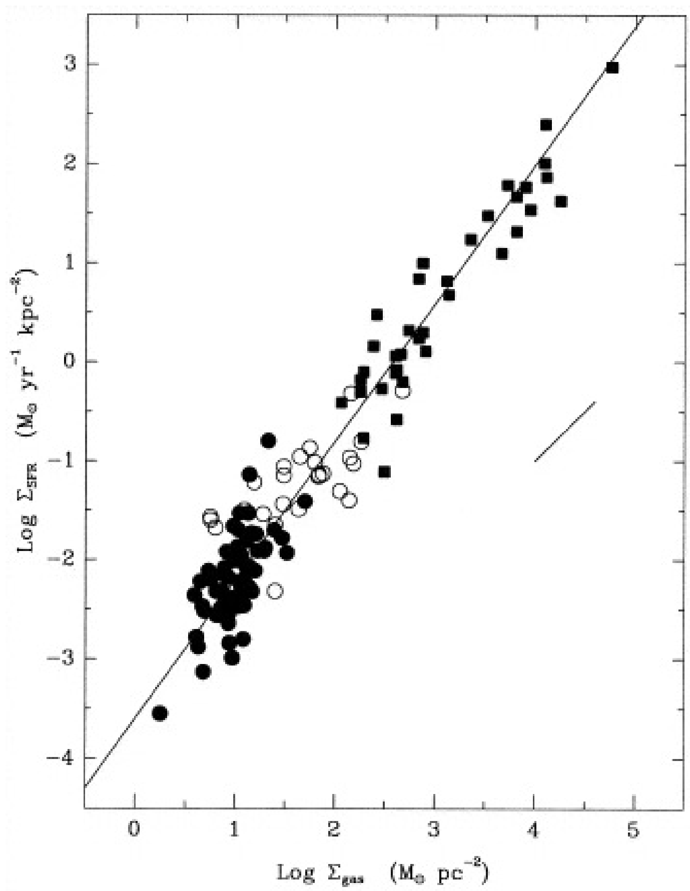

Figure 1.2: Total gas (HI and H_2) Kennicutt-Schmidt relation for 61 normal spiral galaxies (black circles) and 36 infrared starbursts (black squares) (Kennicutt 1998). The open circles represent the centers of the spiral galaxies. The least-squares fit has an index N = 1.4.

spiral centers (open circles), and starburst galaxies (black squares). The ability to fit a wide range of parameter space to a single power provides a very clear path to understanding and interpreting the relationship between forming stars and the gas content of a galaxy, and a recipe for simulations to follow (Kennicutt 1998). However, the author cautions against relying on a single explanation for the observed relationship - no matter how simple and tempting it may be.

Another work making efforts to understand star formation is Lin et al. (2019), which characterises a 3D log-linear relation between molecular gas surface density, star formation surface density, and stellar mass surface density. They argue that these 3 quantities together are all tightly correlated, though they suggest the Kennicutt-Schmidt (KS) relation is one of the more well-defined correlation. In addition to the data from Gallagher et al. (2019), I use the relation from Lin et al. (2019) for a more in-depth understanding of normal spiral galaxies for comparison to my sample.

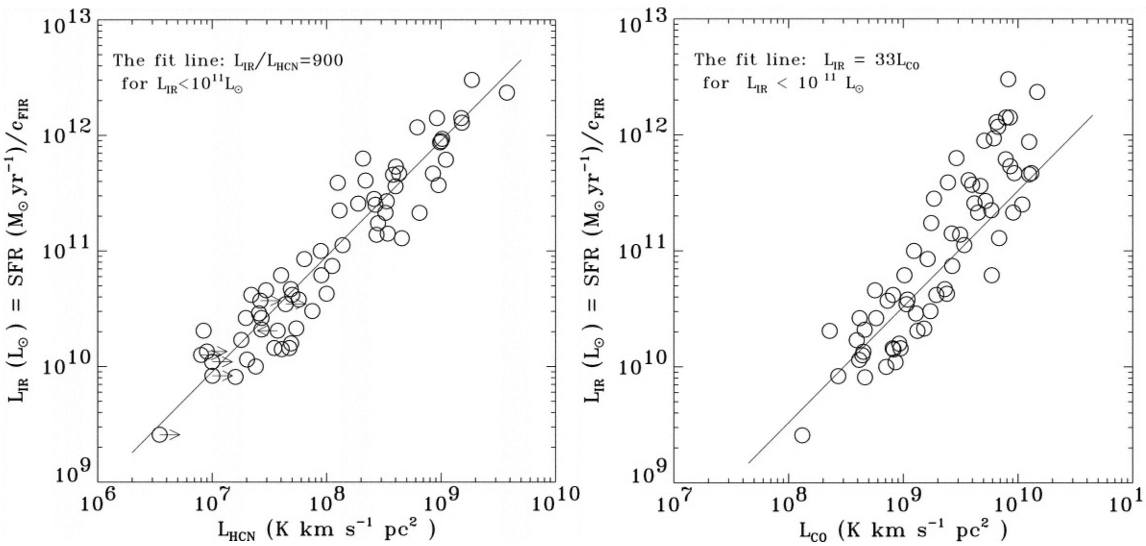

(a) (b)

Figure 1.3: (Left) A dense gas Kennicutt-Schmidt law relation for 34 normal spiral galaxies, 22 LIRGs and 9 ULIRGs (Gao and Solomon 2004). They find one fit to the lower end of the luminosity extends to the entire sample. (Right) A Kennicutt-Schmidt law relation for 34 normal spiral galaxies (open circles), 22 LIRGs and 9 ULIRGs (black circles) (Gao and Solomon 2004). They find the fit to the lower luminosity galaxies does not extend well to the higher end of the sample.

Kennicutt (1998) fit power laws between the SFR and the total gas or molecular content of a sample of galaxies. In 2004, Gao and Solomon adjusted this recipe to apply it exclusively to dense molecular gas ($n(H_2) \geq 3 \times 10^4$ cm^{-3}), which is associated with giant molecular clouds (GMCs), a hotbed of star formation. With global data from 9 ultraluminous infrared galaxies (ULIRGs), 22 LIRGs, and 34 spirals they compare infrared data as a SFR tracer to carbon monoxide (CO) and hydrogen cyanide (HCN) luminosities. By fitting the lower brightness end of the samples with slopes at unity, they find a more constant power-law that extends into the starburst regime with HCN luminosity, while not reproducing a single accurate fit with CO. By fitting the lower luminosity galaxies IR and HCN luminosity, they find the fit between IR and HCN in the lower luminosity galaxies is consistent with more extreme galaxies, and this is also reflected in the global measures of star formation and dense gas mass. They do not find trend lines fitted to the low end of CO luminosity extending to the higher end correctly, which they emphasize in the global molecular gas measurement by providing a fit to the lower end and to the entire data set. They conclude that the relationship between IR and CO luminosity may be an indirect result of genuine relationships between IR-HCN, and HCN-CO.

Newer studies such as Usero et al. (2015) have continued examining the relationship between dense gas and star formation. They focused on the disks of normal star forming spiral galaxies, with the Institut de radioastronomie millimétrique (IRAM) 30 m telescope observations of 29 nearby spirals at about 1.5 kpc resolution. Importantly, they find that areas of high dense gas fraction preferentially exist in areas containing higher amounts of molecular gas than atomic gas (Usero et al. 2015). On the other hand, it seems the ratio of IR/HCN luminosities (related to the SFE of dense gas, or inverse depletion time of dense gas) and molecular-to-dense gas ratios have an inverse relationship; SFE$_{dense}$ decreases in areas of high $\Sigma_{dense}/\Sigma_{mol}$. This could potentially be due to changing environmental factors within galactic disks; which would require adopting conversion factors that vary within a galaxy (Usero et al. 2015). They conclude that a simple star formation model which assumes gas over a certain density threshold produces stars - used by many - cannot be the entire story. I do not apply any of the advanced star formation models presented in Usero et al. (2015), though in the long run these alternative models may provide a clearer and more accurate framework for interpreting the data presented in this work.

Gallagher et al. (2018) also discuss similar findings regarding star formation models. They present Atacama Large Millimeter/submillimeter Array (ALMA) data of the inner regions of 4 local galaxies across multiple lines such as, but not limited to, HCN(1-0), HCO^+(1-0), and star formation tracers. They also supplement their data with other surveys such as EMIR Multiline Probe of the ISM Regulating Galaxy Evolution (EMPIRE), archival CO maps, HCN maps from other works, and more. Like Usero et al. (2015), Gallagher et al. (2018) find that the SFE of dense gas decreases in regions of high molecular gas surface density. This is shown in Figure 1.4 (Figure 10 from Gallagher et al. 2018), with multiple galaxies and the Usero et al. (2015) dataset all systematically decreasing with surface density.

The data archive provided at Gallagher et al. (2019) is used in this thesis to extend the sample of data available, and to provide a wider context in which to analyze and interpret our own data consisting entirely of U/LIRGs.

There have also been studies attempting to point more closely at U/LIRGs specifically. García-Burillo et al. (2012) studied 19 LIRGs observed by the IRAM 30m telescope in HCN(1-0), CO(1-0), mid IR (star formation tracer), and more. In terms of a standard Kennicutt-Schmidt relation, they find that there is likely a bimodal distribution between normal spirals and U/LIRGs (see Figure 1.5), and comment that obscured star formation and adjustments to conversion factors may exacerbate this

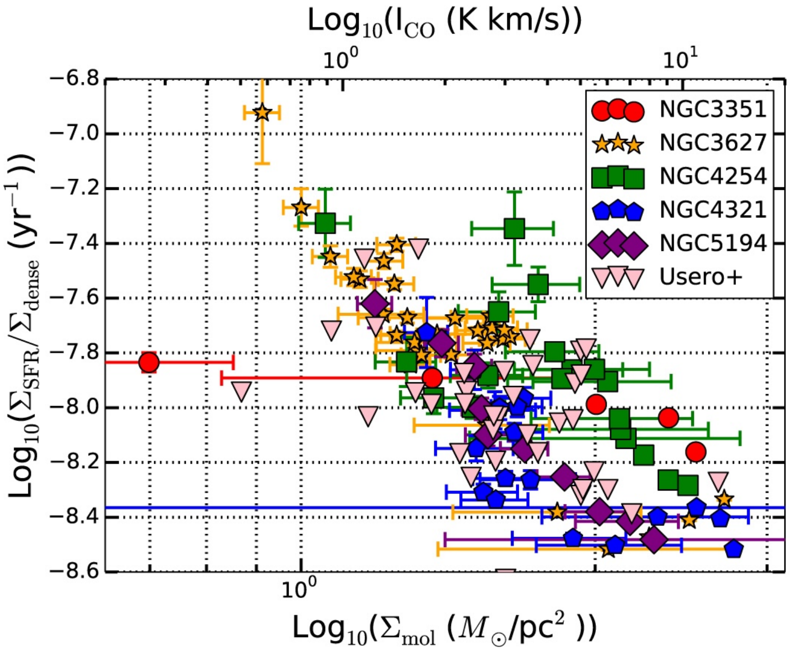

Figure 1.4: Relationship between SFE$_{dense}$ and molecular gas surface density (Gallagher et al. 2018). Dense gas becomes less efficient in star formation at higher surface densities.

difference. Additionally, they report that the SFE of dense gas is 3-4 times greater in U/LIRGs.

Wilson et al. (2019) also analyzed 5 U/LIRGs with highly-resolved data from ALMA, finding a much steeper slope of 1.74 for the standard KS relation than the nearly linear value found in previous projects. They find that the depletion time of the bulk gas decreases with higher surface density, thus the star formation becomes more efficient. Figure 1.6 from Wilson et al. (2019) explores two different fits for the KS relation in these U/LIRG galaxies. One is a bimodal distribution which is steeper at the higher surface densities, and the other is a single power-law fit. The inference that the KS relationship may be steeper at higher surface densities - especially in starbursts or galactic mergers - is a common theme.

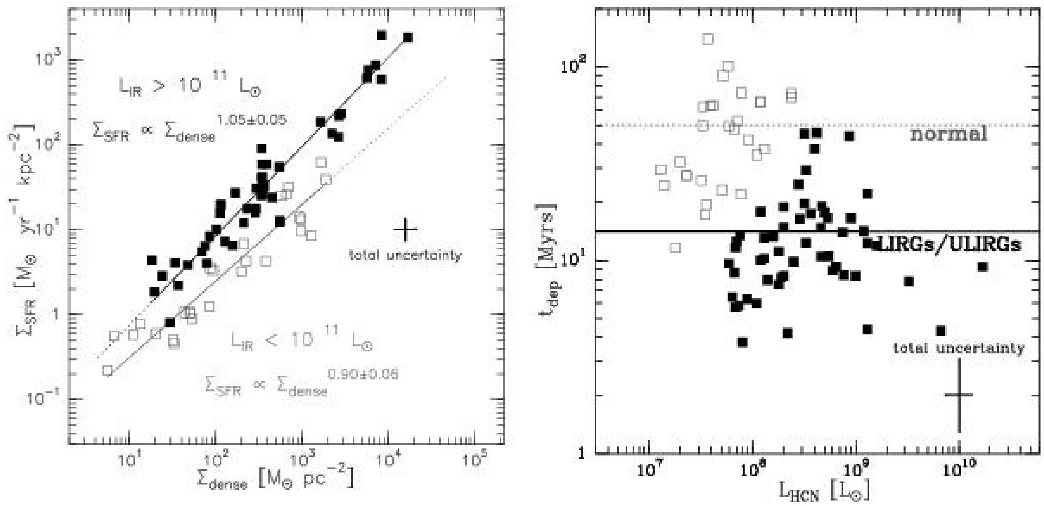

Figure 1.5: (Left) Dense gas KS relation of spirals (open squares) and U/LIRGs (black squares) (García-Burillo et al. 2012). There are two labeled fits, the fit for U/LIRGs being slightly steeper, but different with statistical significance. (Right) depletion times for that sample against the luminosity of the dence gas tracer, L_{HCN}. They find systematically lower depletion times for U/LIRGs (García-Burillo et al. 2012).

1.4 CN as a Tracer for Dense Gas

An important factor that is missing for about half of the sample of galaxies used in this thesis is access to the commonly used dense gas tracer HCN (J=1-0). This tracer is normally required to characterize quantities such as the surface density of dense gas and the dense gas fraction ($f_{dense} = \Sigma_{dense}/\Sigma_{mol}$). This work uses CN (cyanide, N=1-0) in place of HCN. The justification for this comes from the work of Wilson et al. (2023) and Ledger et al. (2023) who discuss the potential to use the molecular line emission of CN as a dense gas tracer. CN has 9 hyperfine lines that come in two groupings which are commonly referred to CN_{bright} and CN_{faint} (Ledger et al., 2023). The strongest evidence is found in Figure 1.8 (Figure 2 in Wilson et al. 2023), which presents a ratio between the luminosity of the two related molecules - I_{CN}/I_{HCN} -

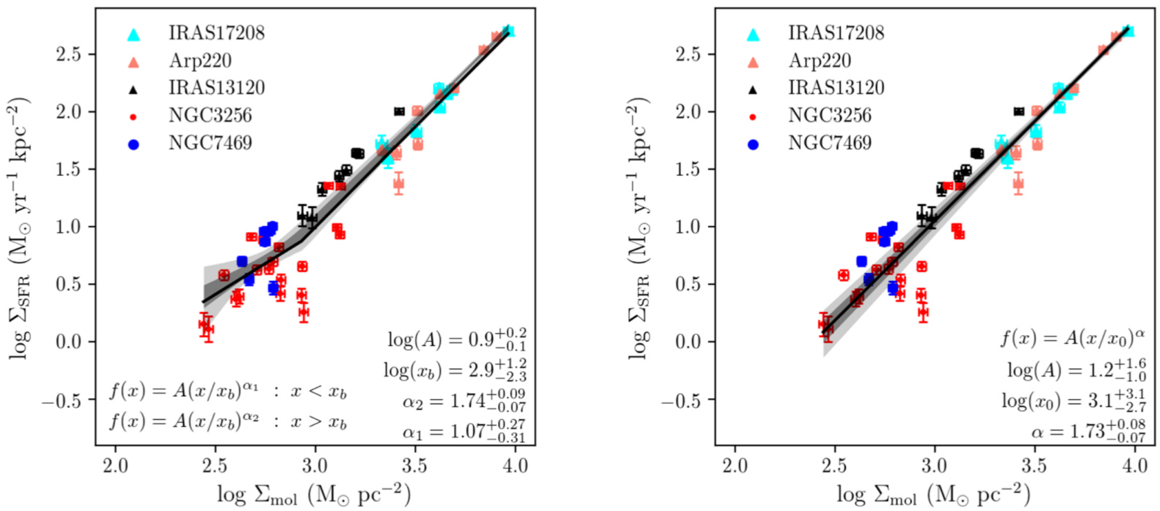

Figure 1.6: (Left) KS relation of 5 U/LIRGs with a bimodal fit (Wilson et al. 2019). (Right) Single fit of the same data (Wilson et al. 2019). In either case, the fit slope is greater than 1 at high surface density.

which is measured to be constant over many dex in gas or SFR surface density. The conclusion reached in that paper is that the CN molecule is a viable tracer for dense gas, as its brightness would be directly proportional to that of the standard dense gas tracer, HCN. Ledger et al. (2023) discuss in detail the sample of 12 LIRGs and 4 ULIRGs, the sample which is adopted for this thesis.

1.5 Goals

This thesis examines the process of star formation in the sample of 16 U/LIRGs from Ledger et al. (2023). This kind of analysis has been done by authors such as Usero et al. (2015), who studied the disks of normal star forming spirals, or Wilson et al. (2019), who studied 5 U/LIRGs - though without access to dense gas data. Compared to this previous work, this thesis is a novel study of resolved star formation in a much more substantial sample of U/LIRGs, and examines the driving factors behind the star

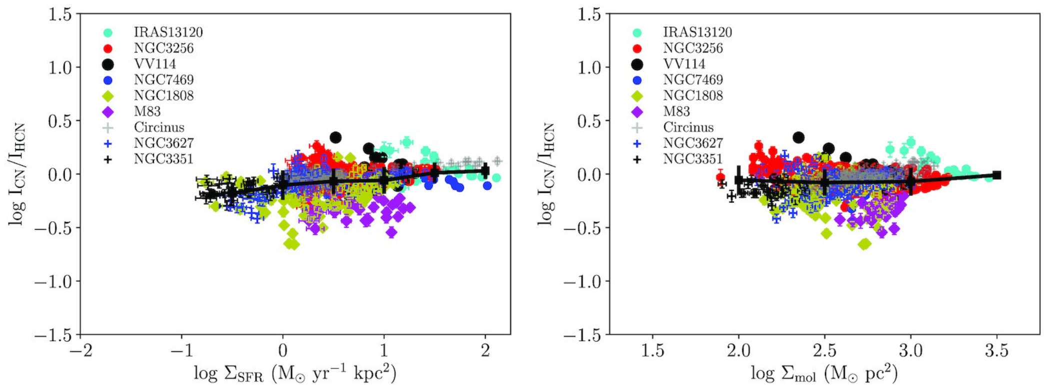

Figure 1.7: (Left) I_{CN}/I_{HCN} showing a constant relationship with scatter over multiple magnitudes of SFR and in both spirals (crosses and diamonds) and U/LIRGs (circles). (Right) The ratio is still constant over many magnitudes of Σ_{mol}.

formation process. Chapter 2 discusses the data used for this work and the methods taken to carry out the analysis. Chapter 3 describes results brought about through the analysis and interpretations of the data by examining correlations between various observed quantities. The final chapter discusses a summary of the work and potential directions this line of research can take in the future.

Chapter 2

Data and Methods

2.1 Sample Selection

For this work I adopt the sample from Ledger et al. (2023) in order to examine resolved star formation and CO $J = 1 - 0$ and CN $N = 1 - 0$ molecular lines. This sample contains 4 ULIRGs and 12 LIRGs, all extremely active galactic environments, such as starbursts and galactic mergers, compared to a regular spiral such as the Milky Way. The sample is derived from the Herschel Ultra Luminous Infrared Galaxy Survey (HERUS, Pearson et al. 2016) and Great Observatories All-sky LIRG Survey (GOALS, Armus et al. 2009) samples (Ledger et al. 2023). For sample selection the requirements were that the data exists in the ALMA archive with redshift $z < 0.05$, has coverage in CO and CN (both 1-0 transition) and 500pc or better resolution. For details and project codes refer to Ledger et al. (2023). For the purposes of this thesis the integrated intensity maps for CO and CN from Ledger et al. 2023 are used in the analysis. In Table 2.1 the sample is listed in order of descending radio luminosity. The radio luminosities are calculated using equation 2.4.1 (Solomon and Bout 2005).

Galaxy[a]	Distance (Mpc)	log L_{radio} ($L_\odot$ Hz^{-1})	log L_{IR} $L_\odot$
IRAS 13120-5453	137	-3.648	12.28
ARP 220	81.1	-4.026	12.21
NGC 6240	106	-4.410	11.85
IRAS F10565+2448	194	-4.457	12.07
IRAS F18293-3413	77.2	-4.462	11.79
IRAS F05189-2524	188	-4.581	12.16
NGC 7469	66	-4.591	11.59
NGC 3256	44.3	-4.634	11.75
NGC 2623	83.4	-4.780	11.59
NGC 1614	67.9	-4.786	11.65
NGC 3110	77.8	-4.935	11.35
ESO 320-G030	50.7	-5.021	11.35
NGC 1068	13.97	-5.104	11.29
NGC 5104	84.6	-5.137	11.21
NGC 4418	35.3	-5.343	11.16
NGC 1365	19.57	-5.425	11.08

Table 2.1: The full list of the sample used in this thesis in order of decreasing radio luminosity. The radio luminosities are measured using apertures in CARTA. The infrared luminosities and distances are adopted from Ledger et al. (2023).

a Galaxies ordered by radio luminosity

2.2 Imaging the Radio Continuum Data

The Physics at High Angular resolution in Nearby GalaxieS (PHANGS-ALMA) pipeline is a tool described in detail in Leroy et al. (2021) that is used for calibrating raw data from the ALMA array, carrying out continuum subtraction, and imaging the data in various formats. It allows for streamlined use of Common Astronomy Software Applications (CASA, version 5.6.3 used for this thesis) (McMullin et al. 2007) and easier creation of science-ready data products. One of the works I build upon in this thesis is that of the work of Ledger et al. (2023). Therefore, I apply PHANGS-ALMA pipeline with similar methodology for consistency between the creation of line products from their work and continuum products from this thesis.

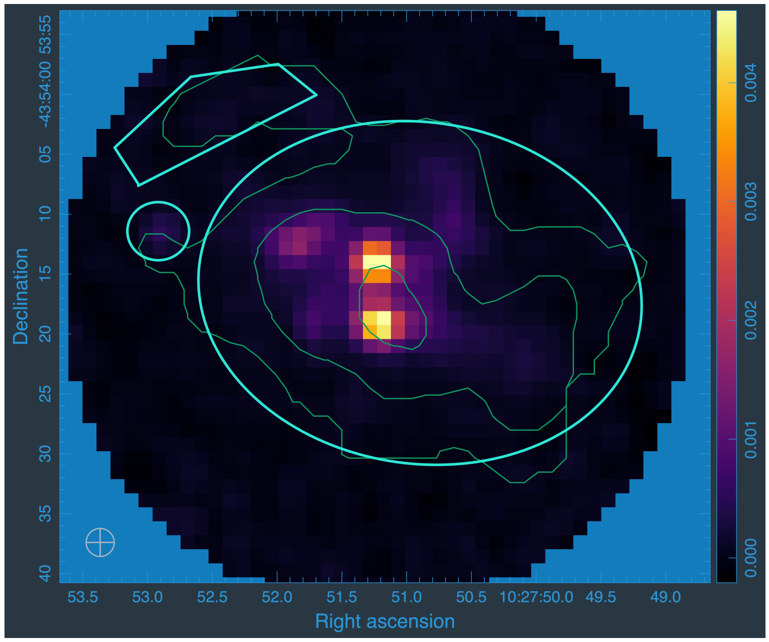

Figure 2.1: CARTA image of NGC 3256. The thin green lines are contours drawn from the CO (J=1-0) emission line moment 0 map. The blue apertures are drawn by hand taking into consideration the contour lines and continuum emission brightness. In this case, 3 apertures were drawn to cover all relevant emission.

The imaging pipeline, specifically, is the portion of the pipeline relevant for this thesis. The data I started with had already been calibrated for use at NAOJ (National Astronomical Observatory of Japan). This project required the use of 2 pipeline functions: staging and imaging. Staging refers to compiling all the necessary UV data files and imaging refers to CASA executing a reverse Fourier transform to convert the UV data to a 2-dimensional image, with a third dimension in the form of velocity channels for molecular lines. The pipeline products of relevance for this thesis project are the images which contain the radio continuum emission strength, without signal from any molecular emission lines or other contaminants. This emission at approximately

110 GHz is dominated by free-free emission, and is used to estimate the star formation rate (Murphy et al., 2011), as described in Section 2.4. The PHANGS-ALMA pipeline was used to image 15 out of the 16 galaxies in the sample of U/LIRGs. NGC 1068 is the one galaxy for which the calibrated UV data was not publicly available. The continuum image of this galaxy was acquired directly from Toshiki Saito (private communication). The initial beam was much smaller than the size we smoothed it to - going from 0.759638" $\times$ 0.66433" to 7.38" $\times$ 7.38" - a significant amount of smoothing. After acquiring the image it was processed similarly to the rest of the sample to match the line images of the galaxy from Ledger et al. (2023).

In order to use these continuum maps for this project, two things are required: smoothing the continuum, and matching the map formatting to that of Ledger et al. (2023) for comparison. The program used for this is once again CASA version 5.6.3. Firstly, the continuum image is smoothed to a rounded beam with the same shape and size for each galaxy, rather than the varying elliptical beams. The necessity of rounding the beams is to ensure that the resolution for all galaxies is 500pc for data analysis. Additionally, the size of the image pixels was binned to half that diameter: 250pc. This size scale typically contains a few molecular clouds (Ledger et al. 2023). However, it is also necessary that the coordinates for the radio continuum images match the moment maps for the CO J= $(1-0)$ and CN N= $(1-0)$ lines provided by Ledger et al. (2023). CASA allows for reformatting of images, so the images were regridded to the formatting of the molecular line moment 0 maps. The various signals, such as free-free emission or CN line emission, in this format can be compared directly in each pixel. Continuum images for all galaxies are shown in Figure 2.2a and 2.2b. The color bar is spectral flux in units of milli-Janskys/beam (mJy/beam).

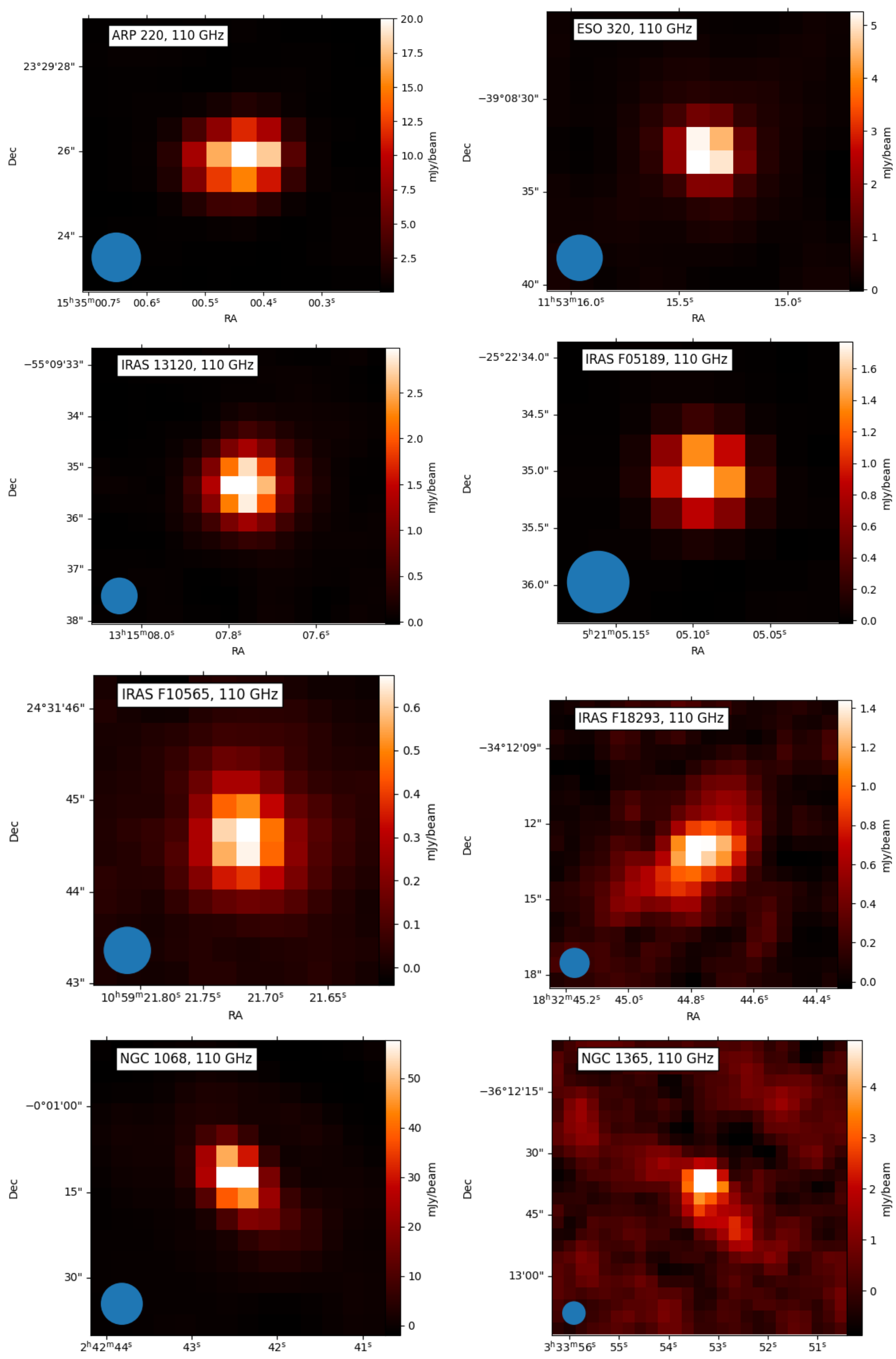

Figure 2.2a: 110 GHz continuum image of the galaxies in this sample. The beam (in blue) is approximately 500 pc across, with the pixels at 250 pc.

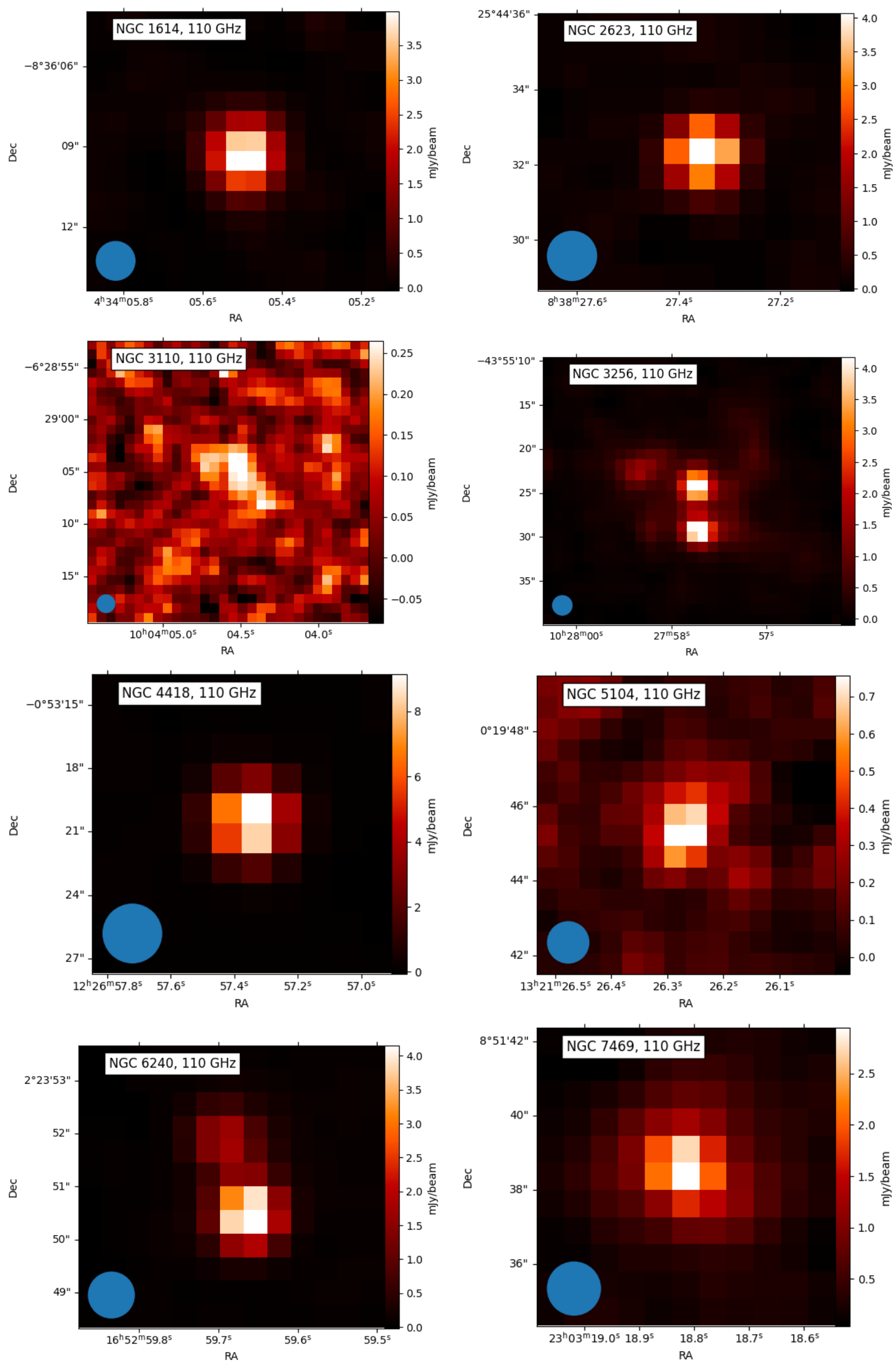

Figure 2.2b: Continued from Figure 2.2a

2.3 CO and CN maps

The intensity maps for CO and CN emission for this thesis are adopted from Ledger et al. (2023). They had or were provided images for some galaxies (IRAS 13120-5453, NGC 1068, NGC 6240), and the rest were continuum subtracted and imaged with the PHANGS-ALMA pipeline v3 (Leroy et al. 2021). In the continuum subtraction, the CO line and CN hyperfine lines were excluded in order to retain as much signal as possible. Following the creation of the image cubes, any further processing was done manually. Examples of manual processing were smoothing the beam of the images (function: imsmooth) to 500 pc or regridding the images (function: imregrid) to 250 pc pixel size.

In order to create the products for CO (1-0), the Sun moment map method was applied (Sun et al. 2018, Sun et al. 2020, Ledger et al. 2023). This method involves the creation of noise cubes for the galaxies which are used to measure RMS noise in channels with no CO (1-0) signal for each pixel (Sun et al. 2018, Sun et al. 2020, Ledger et al. 2023). Initially the mask in the CO (1-0) map includes all pixels with positive signal and requires that the signal-to-noise (S/N) is at least 4 in the channels following and preceding the current one (Ledger et al. 2023), meaning the signal must be significant in both the current channel and its adjacent channels. Then the requirements are eventually lessened to go down to a S/N of 2 (Rosolowsky and Leroy 2006, Sun et al. 2018, Sun et al. 2020, Ledger et al. 2023), masking out any pixels that do not meet the criteria. The uncertainty for these maps were calculated by using the RMS noise cubes and multiplying each pixel by the number of channels used in the moment maps and the channel width (Ledger et al. 2023), described by the equation they present:

$$\sigma_{pix} = \sigma_{RMS} \times \sqrt{N_{chan}} \times \Delta V. \quad (2.3.1)$$

With this equation they were able to make uncertainty maps for the CO (1-0) signal (Ledger et al. 2023).

The CN (1-0) products were made with a spectral shuffle and stack method (Schruba et al. 2011, Leroy et al. 2016, Ledger et al. 2023). Initial masks only include pixels where CO emission is present in CO data cubes. The reason for this is that Ledger et al. 2023 expected no weak CN emission without the presence of CO, as CN emission is much dimmer. The CN spectrum for each pixel is shifted by the corresponding CO velocity from a moment 1 map (velocity map). Then, using the CO linewidth from the moment 2 CO map, the CN spectrum is masked to only contain signal within 3 $\times$ the CO spectral linewidth. This signal is then integrated to obtain an intensity in each pixel, leading to a moment 0 map for both the CN bright and CN faint line groupings. The uncertainty maps are created in the same way as the CO uncertainty maps were created.

2.4 From Observables to Physical Quantities

Upon creating the radio continuum emission maps for all the galaxies in the sample, the data is converted to physical quantities: molecular gas surface density (Σ_{mol}), star formation rate surface density (Σ_{SFR}), etc. The conversion to physical quantities and subsequent plotting was all done in python script. For molecular lines, a deceptively simple method is used: a conversion factor that takes the integrated intensity of a particular emission line to a column density, for example, $\Sigma_{mol} = \alpha_{CO}(I_{CO,J=1-0})$. Multiple calibrations of the conversion factor exist depending on environment (Bolatto et al. 2013). This thesis adopts the conversion factor for the CO $J = 1-0$ line $\alpha_{CO} = 1.1$ used for U/LIRGs (Bemis and Wilson 2023), a factor of 4 smaller than normal disk galaxies like the Milky Way. The sample in this thesis is comprised of gas rich, dusty galaxies, where the vast amounts of gas exist in higher densities and temperatures and reach excited states more easily (Bemis and Wilson 2023, Downes et al. 1993, Bolatto et al. 2013). The conversion factor is assumed to be constant throughout the sample and spatially across each galaxy. However, this prescription could be varied for each galaxy and indeed within them to yield more accurate measurements reflecting the galactic environment rather than using an "average" conversion factor (Bemis et al. 2024).

Again from Bemis and Wilson (2023) the adopted ratio between HCN and CO is $\alpha_{HCN}/\alpha_{CO} = 3.2$, to approximate the conversion factor of HCN $J = 1-0$. This HCN line is typically used to estimate dense gas, which is defined in this thesis as densities $> 10^4 cm^{-3}$. Since half of the galaxies in the sample do not have HCN data available, we use CN $J = 1-0$ instead. Wilson et al. (2023) suggest that CN is a valid tracer of dense gas due to its constant ratio with HCN across many paramater spaces. The average ratio across the 9 galaxies in their sample of spirals and U/LIRGs is $I_{CN}/I_{HCN} = 0.86$. In order to use the CN data the I_{CN}/I_{HCN} ratio is applied, yielding a calibrated α_{CN} used to convert integrated intensity measurements to dense gas surface density, Σ_{dense}.

In turn, star formation rate estimates are done in two main steps. The continuum maps from the PHANGS-ALMA pipeline v3 contain data in units of Janskys per beam (intensity I_{110GHz}, later converted to specific flux S_{110GHz}). The flux is acquired in Cube Analysis and Rendering Tool for Astronomy (CARTA) through drawing apertures on the radio continuum images guided by CO contour lines from the CO moment 0 maps. An example of this process is shown in Figure 2.1. This method was applied in order to encompass the continuum emission in any area where star formation may be occurring by outlining the majority of signal from the bulk gas tracer, in other words, areas where there is "fuel" for star formation in the form of molecular gas. Using an equation from Solomon and Bout (2005) it is possible to convert to specific luminosity (L_{110GHz}),

$$L_{\nu rest} = 4\pi D_L^2 (1+z)^{-1} S_\nu, \tag{2.4.1}$$

where D_L is the distance to the source, and S_ν is the flux. This then needs to be converted to star formation rate with an equation from Murphy et al. (2011),

$$SFR_\nu = 4.6 \times 10^{-28} (\frac{T}{10^4 K})^{-0.45} (\frac{\nu}{GHz})^{0.1} L_{\nu rest}, \tag{2.4.2}$$

where T is the excitation temperature of an electron, ν is the frequency (110 GHz) and $L_{\nu rest}$ is the calculated specific luminosity. All pixels in continuum maps with a signal less than 5σ were excluded from analysis. The noise in the continuum maps is estimated by drawing apertures away from the central source and averaging this baseline emission over multiple different apertures. The error in the molecular emission lines is taken from Ledger et al. (2023).

Chapter 3

Results and Discussions

In the figures shown in this thesis, the sample is divided into LIRGs and ULIRGs for plotting, with 2 notable exceptions. The first is NGC 3256, which seems to set a noise floor in Σ_{SFR} for this sample, visible in Figure 3.5, where there is a set of points approaching what seems to be a lower limit in SFR. NGC 1068 is the other galaxy highlighted. It often contains data points that appear to be outliers when compared with the rest of the sample, and will be discussed in Section 3.2. Wilson et al. (2019) show a trend in the KS relation for a similar sample of U/LIRGs, which is included in this thesis' KS law plot in Figure 3.5. For further context, data from Gallagher et al. (2018) is included, which consists of ALMA data of normal spiral galactic disks. This allows me to place the U/LIRG measurements within the context of the broader field of galaxies. Lastly, a trendline from Lin et al. (2019) is shown for the KS relation of regular spirals. The plots and interpretations of them are discussed in the following sections.

3.1 Efficiency Maps

Chapter 2 presents 110 GHz radio continuum maps for the entire sample of U/LIRGs, which probe the star formation in each of the 16 galaxies. Also outlined in the previous chapter are the methods with which free-free emission is converted to a SFR surface density estimate, and CO and CN line emission converted respectively to bulk and dense molecular gas surface densities. It is now possible to examine, on a pixel-by-pixel basis, where stars are forming most quickly and efficiently. Measures of such values - instantaneous depletion time, for example - are often estimated through ratios of Σ_{gas} and Σ_{SFR} (Usero et al. 2015, Wilson et al. 2019). This work will often discuss the SFE, both for the bulk and dense molecular gas, which is given by the ratio

$$SFE = \frac{\Sigma_{SFR}}{\Sigma_{gas}}. \tag{3.1.1}$$

The SFE maps for this sample systematically yield SFE$_{dense}$ higher or equal to SFE$_{mol}$, which falls within expectations as Σ_{dense} should be smaller than Σ_{mol}. It is important to note this is not a true efficiency of stars formed over long periods, but rather has units of time^{-1}, and so it is a proxy for understanding the efficiency with which gas is converted into stars. Another common way to discuss this is depletion time, which is simply the inverse of SFE. Instantaneous depletion time is an estimate of the amount of time required for all the gas present in a galaxy to collapse into stars, assuming the SFR does not change as the fuel is consumed.

Figure 3.1 presents the SFE maps of NGC 6240 for both bulk and dense molecular gas. On a pixel-by-pixel basis, the maps show similar peaks and valleys of SFE, but with systematically higher values in the SFE$_{dense}$ map. This general trend is relatively consistent across the entire sample. While the peak or minimum SFE pixels for the bulk and dense molecular gas may not correspond exactly in every single galaxy, most pixels reflect higher efficiency for conversion of dense gas to stars compared to bulk molecular gas. IRAS 13120-5453 has slightly higher SFE_{mol} at and around the galactic centre, although the peaks do not match between the two maps. Lastly, IRAS F05189-2524 has higher SFE_{mol} at the very centre pixel. These figures are included in Appendix A.

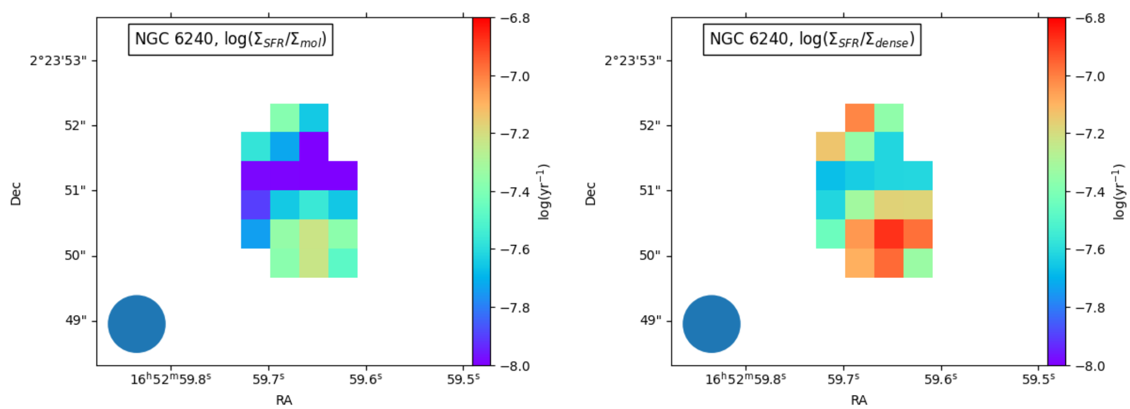

Figure 3.1: (Left) SFE_{mol} map for NGC 6240. (Right) SFE_{dense} map for the same galaxy. The peaks and low points exist in the same pixels, but are systematically higher for the SFE_{dense}.

Figure 3.2 contains another set of SFE maps, this time for NGC 3256. In this case, it remains true that every pixel in the SFE_{dense} map reflects a higher efficiency of converting gas to stars than any pixel in the SFE_{mol} map. However, in the SFE_{mol} map, the northern and southern nuclei show similar levels of efficiency for converting bulk gas into stars, while the northern nucleus is significantly less efficient than the southern nucleus in converting dense gas into stars in the SFE_{dense} map. An additional complication exists due to the active galactic nucleus (AGN) present in the southern nucleus. It is difficult to determine whether the dense gas is being traced correctly or if the AGN feedback affects excitation temperatures of CN or HCN.

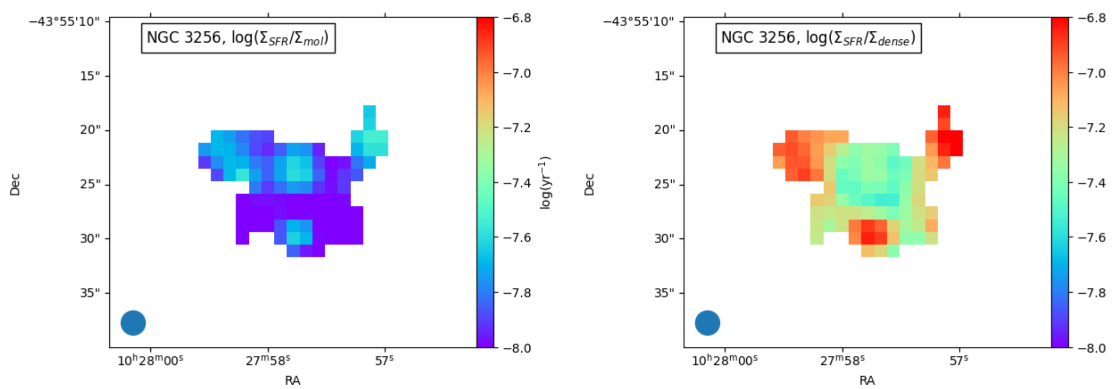

Figure 3.2: (Left) SFE$_{mol}$ map for NGC 3256. (Right) SFE$_{dense}$ map for the same galaxy. The SFE$_{dense}$ contains the same peaks except for the northern nucleus, which contains a higher SFE than the bulk molecular gas version, but is not a peak relative to the southern nucleus or other areas with high SFE.

In this U/LIRG sample, the peaks in SFE align tend to align with peaks in the SFR as traced by the radio continuum. An important caveat to note is that many galaxies in the sample contain an AGN. This will enhance the radio continuum emission in the central region in each galaxy that contains an AGN, leading to an overestimation of SFR. AGN can also affect Σ_{mol} and Σ_{dense} estimates by heating gas and making tracers such as CO and CN brighter per unit mass, meaning adjustments to the conversion factors may be needed. Not only can this lead to misinterpreting SFE maps, but also attempts at characterizing star formation - one of this thesis' goals.

3.2 Physics of Star Formation

Chapter 1 discusses papers that have attempted to characterize the physics driving the star forming process such as Usero et al. (2015), Gallagher et al. (2018), and

Wilson et al. (2019). In order to build upon this and glean information on the causes driving star formation, this work presents analysis of the physical properties of the gas available to form stars and how it correlates with the SFR and other related attributes.

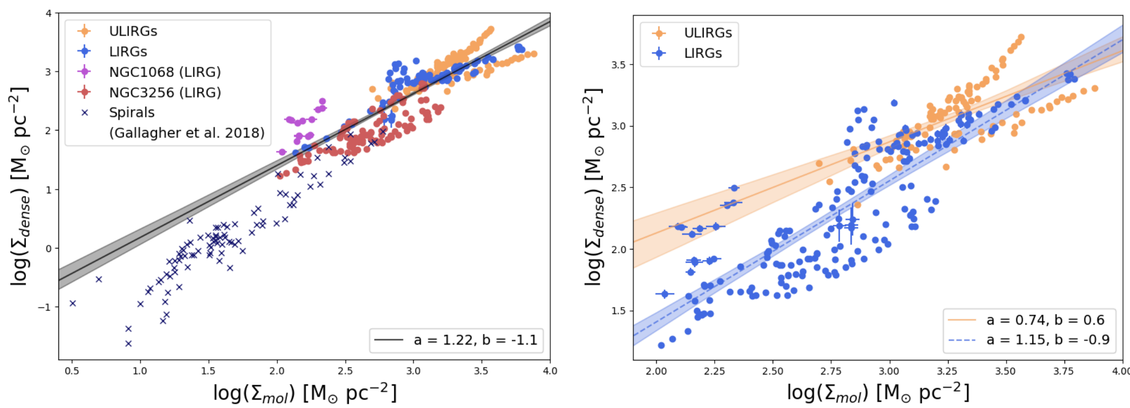

Figure 3.3: Surface density of dense molecular gas plotted against bulk molecular gas. (Left) Black LinMix fit covers the U/LIRG data, with the spiral data from Gallagher et al.(2018) lying entirely beneath the fit. (Right) Zooming in on the U/LIRG sample and separating LIRGs from ULIRGs, with their own fits. The individual fits are shallower than the combined fit on the left.

Figure 3.3 presents a comparison of the dense ($> 10^4$ cm^{-3}) and bulk molecular gas surface densities. It suggests a power-law relationship and perhaps understandably, more bulk molecular gas predicts more dense gas as well. There is a possibility of a forked distribution at the highest end, although that is difficult to determine with only 4 ULIRGs - the spread can simply be a consequence of small sample size and 1 galaxy (ARP 220) being affected by its AGN. Notably, the relationship appears continuous between the spirals and U/LIRGs, with significant overlap as the transition occurs from spirals to our extreme mergers and post-mergers. Note that this is despite a discontinuity in α_{CO} and α_{HCN} from spirals to U/LIRGs. The LinMix fit included in the left figure would suggest a super-linear relationship, even though it is fitted only to the 16 U/LIRGs and not the data from Gallagher et al. (2018). Fitting both sets of data would likely result in an even steeper relationship. The right figure separates the LIRGs and ULIRGs, a process repeated for the figures presented later in this thesis, in order to ascertain any notable differences between the two populations. In this case, the LIRGs are fitted slightly super-linearly and the ULIRGs are sub-linear. Interestingly, both fits are shallower than the combined fit in the left panel.

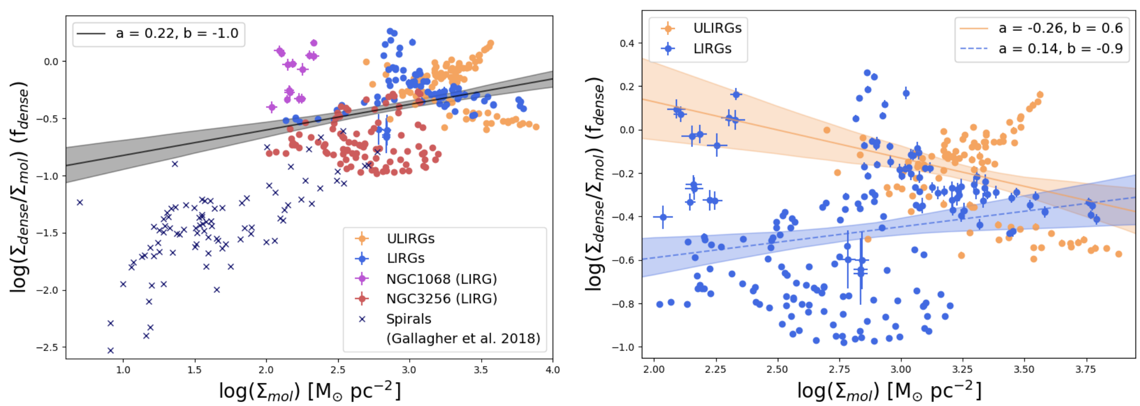

Figure 3.4: Fraction of dense gas plotted against bulk molecular gas. (Left) Black LinMix fit covers the U/LIRG data, with the spiral data from Gallagher et al.(2018) lying entirely beneath the fit, emphasizing what is seen in Figure 3.3. (Right) LIRGs contain quite a bit of scatter, leading to a fit which is very weakly correlated. The ULIRGs yield a negative correlation.

Iterating on this analysis, Figure 3.4 is a comparison of the dense gas fraction f_{dense} against bulk molecular gas. Dense gas fraction is a measure of the relative amount of gas considered dense, represented by the ratio $\Sigma_{dense}/\Sigma_{mol}$. On their own, the U/LIRG sample contains mostly scattered points. The LinMix fit predicts a slight positive correlation between the dense gas fraction and the bulk molecular gas, implying areas rich in star forming material would also have higher fraction of gas available above the threshold required for it to be "dense". The spiral data do not lie on the LinMix fit; however both in Figures 3.3 and 3.4, the context provided by the spiral data suggests there is the potential for one continuous trend between spirals, LIRGs, and ULIRGs. The dense gas fraction being significantly higher on average in the U/LIRGs is particular notable as it is a ratio between two quantities with similar assumptions, making it insensitive to uncertainties in α_{CO} or α_{CN}. On the other hand, some of the brightest signals lead to $f_{dense} > 1$ in some cases, which is not physical. It is likely that accounting for AGN contamination could alleviate most of this. Zooming in specifically on the sample of LIRGs yields a slight positive correlation, with a great deal of scatter. In the ULIRGs, the differences galaxy-to-galaxy lead to slight differences in the fits. The LIRG fit displays a slight positive correlation and the ULIRG a slightly negative correlation, overall yielding a negative relationship.

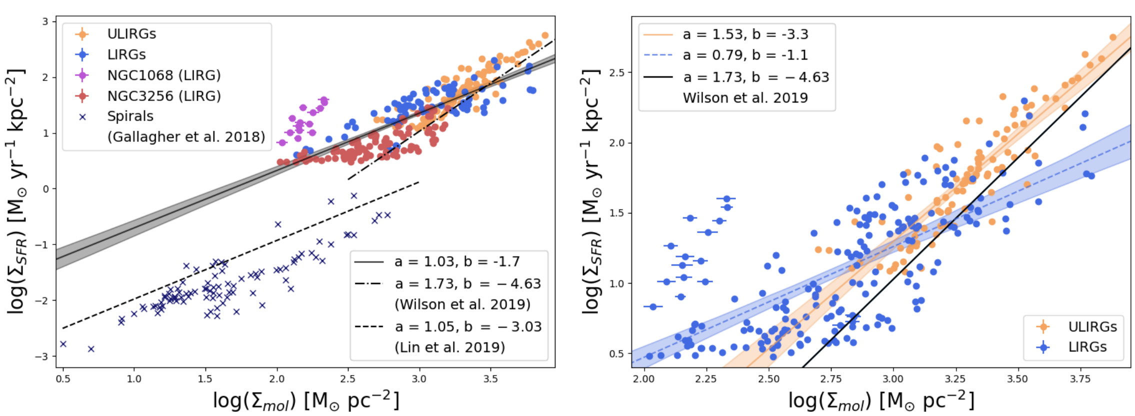

Figure 3.5: Surface density of star formation rate (SFR) against the surface density of bulk molecular gas, known as the Kennicutt-Schmidt (KS) law. (Left) Black LinMix fit for the U/LIRGs results in a nearly linear correlation, parallel to the KS relationship for spirals from Lin et al. (2019) (dashed line). This is contrasted against the much steeper fit from Wilson et al. (2019). (Right) Separating the LIRGs and ULIRGs creates a stark contrast in the slopes. LIRGs end up extremely shallow and the ULIRGs are much closer to the Wilson et al. (2019) slope.

Turning towards SFR, Figure 3.5 characterizes the KS relation for this sample of

U/LIRGs. In addition, the left panel contains spiral data, a fit to 5 U/LIRGs by Wilson et al. (2019), and a fit to spiral data from Lin et al. (2019). The LinMix fit for the sample of 16 U/LIRGs is characterized by a linear slope, similar to the Lin et al. (2019) fit. The major difference is the offset between the two fits. The slope disagrees with the Wilson et al. (2019) fit, which is significantly above linear. The disagreement between the U/LIRG and spiral data could suggest a difference in the underlying physics - assuming a complete and correct set of assumptions. Exploring a bimodal distribution is done in Wilson et al. (2019) where they fit a single line or two separate fits at the low and high end of gas content. The alternative to two different power laws for spirals and U/LIRGs requires calibration of conversion coefficients α, a common theme throughout this chapter.

The right figure focuses on the LIRGs and ULIRGs separately. The LIRG population displays a sub-linear slope, although clearly a positive correlation. On the other hand, the correlation between gas surface density and SFR surface density among ULIRGs is more closely aligned with the fit reported by Wilson et al. (2019). It is important to note that of the sample in that paper, 4 of 5 galaxies overlap with this thesis' sample: ARP 220, IRAS 13120, NGC 3256, and NGC 7469. The first two are ULIRGs, and this work only has four ULIRGs - meaning a similarity in slope to another small sample is not unexpected. Whether the physics observed in Wilson et al. (2019) is different or if conversion factors need to be adjusted on a galaxy by galaxy basis is unclear.

Figure 3.6 depicts a similar relation to the KS relation, this one popularized by Gao and Solomon (2004). Comparing SFR to dense gas surface density rather than bulk molecular gas surface density may be more accurate across different morphologies and yield a stronger correlation (Gao and Solomon, 2004). Indeed, by using a dense gas tracer compared with SFR there is a positive correlation - potentially with a tighter correspondence seen in Figure 3.6 than the regular KS law. Again, there is an offset between the spiral and U/LIRG data, with the spiral data lying completely below the LinMix fit. The fit itself is sub-linear, but a positive correlation nonetheless. In examining the LIRG and ULIRG populations individually, both exhibit positive correlations. The important distinction is that the LIRGs yield a sub-linear power law while the ULIRGs exhibit a distinctly super-linear correlation.

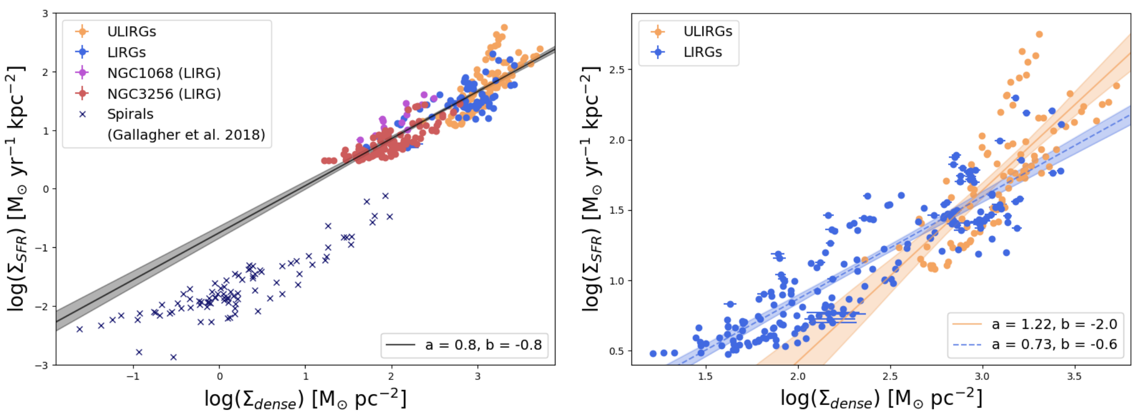

Figure 3.6: Surface density of star formation rate (SFR) against the surface density of dense gas ($> 10^4$ cm^{-3}). (Left) Data seems to correlate more tightly than the regular KS law. Black LinMix fit suggests a slope slightly under linear. (Right) LIRGs and ULIRGs separated, again leading to a significantly steeper slope for the ULIRGs compared to the LIRGs.

Section 3.1 discusses SFE maps and the peaks as they relate to SFR and gas content. Figure 3.7 returns to star formation efficiencies. Rather than assess the relationship of SFE with coordinates in space, the focus is now on the physics affecting SFE in the entire sample. In the left panel of Figure 3.7, there is an offset between spiral and U/LIRG data in both the SFE$_{mol}$ (SFE of bulk molecular gas) and Σ_{mol} parameters. Both datasets appear to be fairly flat in SFE$_{mol}$, corroborated by the

LinMix fit yielding no overall correlation for the U/LIRGs. The efficiency with which gas is forming into stars is much higher in our U/LIRGs - an intuitive result, as many of the U/LIRGs are mergers with starburst regions. On the other hand, discussing the inverse of SFE, depletion times are on the order of 10-100 Myr for the U/LIRGS, with the spirals sitting in the range of 0.3-3 Gyr. Especially true for the spiral data, but also for the U/LIRG data overall, the "efficiency" of converting gas into stars - or alternatively the depletion time - does not depend on the amount of molecular gas present inside each of the two samples. The right panel of Figure 3.7 shows that the LIRGs display a slight negative correlation while the ULIRGs yield just the opposite.

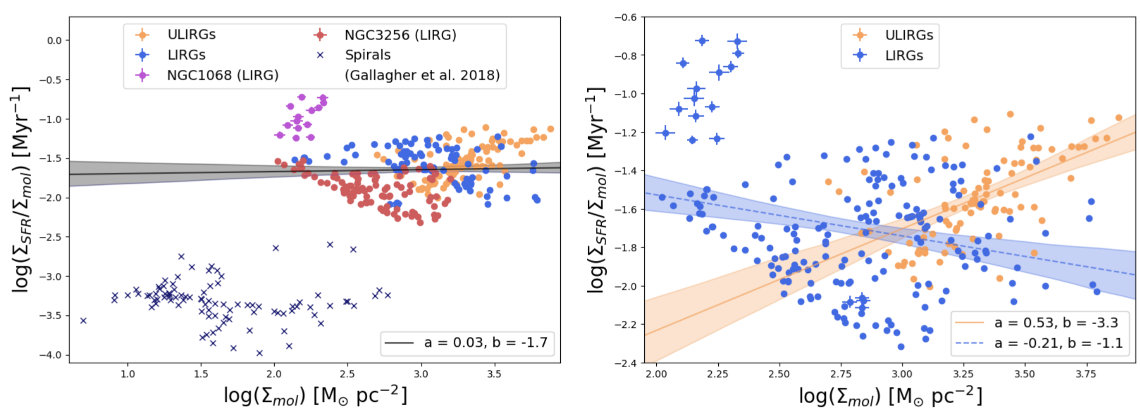

Figure 3.7: Inverse gas depletion time, known also as star formation efficiency (SFE, of bulk molecular gas) against the bulk molecular gas. (Left) LinMix yields a nearly flat fit, suggesting the SFE (or depletion time) is constant. (Right) Individual fits show a slightly negative correlation for the LIRGs and positive one for the ULIRGs.

Figure 3.8 is a similar plot to 3.7, but focusing on dense gas star formation efficiency, which is the inverse of the instantaneous depletion time of the dense gas. There is an obvious slope in this relationship, which retains a distinct offset between the spirals and U/LIRGs for both SFE_{dense} and Σ_{dense}. The similarity is that both samples exhibit a clear negative correlation between SFE_{dense} and Σ_{dense}. What this suggests is that the efficiency of converting dense gas into stars decreases as the amount of gas considered "dense" increases. Alternatively, the depletion time of the dense gas becomes larger with the amount of dense gas. This is rather counter-intuitive, as denser clouds should succumb to gravitational instability more quickly. Therefore, this relationship implies that other mechanisms - a popular one being turbulent feedback - are affecting the star formation. Yet again, the LIRG and ULIRG samples yield opposing correlations, although consistent with what is seen in Figure 3.7. A factor to consider is the 90% confidence range for the ULIRGs is extremely large; a relationship between SFE$_{dense}$ and Σ_{dense} may not be well defined for these ULIRGs.

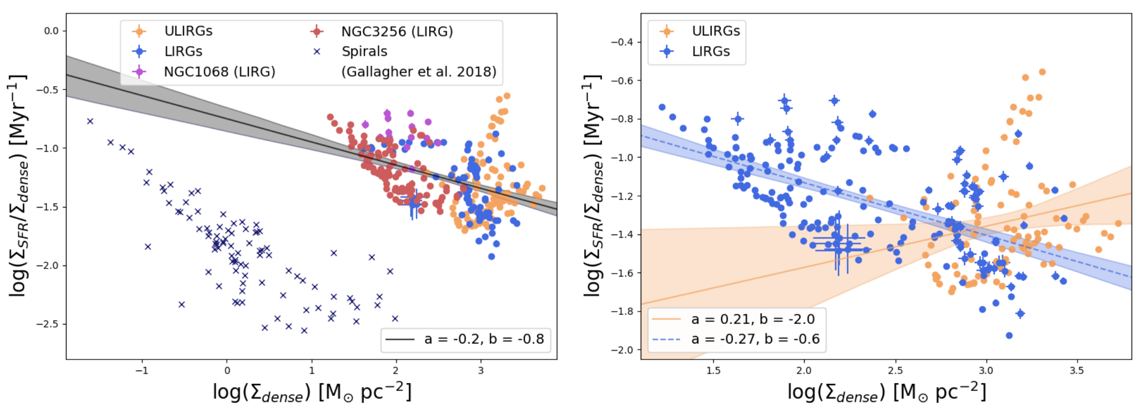

Figure 3.8: SFE$_{dense}$ (or inverse gas depletion time of dense gas) against the dense molecular gas. (Left) LinMix fit shows a weakly negative correlation, suggesting the SFE is lower in denser regions. (Right) Individual fits show a slightly negative correlation for the LIRGs and positive one for the ULIRGs.

The final foray for this chapter is the comparison of SFE$_{dense}$ and f$_{dense}$. Both quantities are ratios, and the dense gas fraction in particular is a quantity for which the terms in the ratio $f_{dense} = \Sigma_{dense}/\Sigma_{mol}$ contain the similar assumptions about conversion between physical quantities and molecular line luminosities (see Section 2.4). Figure 3.9 contains quantities already shown in previous figures, so it is no surprise that the SFE$_{dense}$ and f$_{dense}$ are approximately an order magnitude higher in the U/LIRGs. New information one might infer from the left panel relates to the previous Figures 3.7 and 3.8. The discussion of the previous two plots revealed that the bulk molecular gas did not affect depletion time much - if at all - and more dense gas in turn caused star formation to be less efficient. Similarly, as the ratio of dense to total gas increases, the efficiency of converting dense gas to stars goes down. Alternatively the dense gas depletion time becomes longer with an increase in the dense gas fraction. This is consistent between the LinMix fit of the ULIRG data displaying a slight negative correlation, and the spiral data exhibiting a similar trend. The right panel of Figure 3.9 once again highlights the LIRGs and ULIRGs separately, although in this case both groups of the sample point to a negative correlation. The ULIRG slope is significantly steeper.

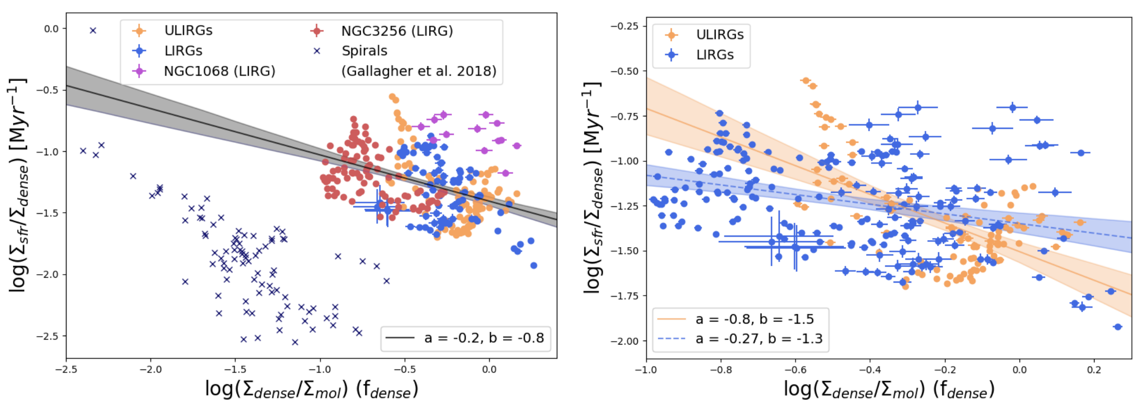

Figure 3.9: SFE$_{dense}$ (or inverse gas depletion time of dense gas) against the fraction of dense molecular gas. (Left) LinMix fit shows a weakly negative correlation, suggesting the SFE is lower in denser regions. (Right) Individual fits show slightly negative correlations for boththe LIRGs and positive one for the ULIRGs, with the ULIRGS being much steeper.

3.3 Discussion

The results in this chapter reveal a systematic increase in SFE$_{dense}$ compared to SFE$_{mol}$ while generally showing these SFE peak at the same location on two-dimensional maps of 10 LIRGs and 4 ULIRGs. The SFE maps for IRAS 13120-5453 and NGC 3256 are directly comparable to similar maps presented in Wilson et al.(2023). In that work, the sample is quite heterogenous, containing the two ULIRGs mentioned, but also starbursts and spiral galaxies. On its own, the systematic increase in the dense star forming efficiency over the bulk molecular gas cannot say much, especially as it is not a true efficiency. However, a related quantity may aid in the interpretation. The efficiency per free-fall time is the ratio between the gravitational free-fall time and the depletion time, $\epsilon_{ff} = \tau_{ff}/\tau_{dep}$. As has been discussed in this thesis, inverse depletion time is also often discussed as SFE, so it is possible to rewrite efficiency per freefall time as $\epsilon_{ff} = \tau_{ff} \times SFE$. Since SFE$_{dense}$ is systematically higher than SFE$_{mol}$, dense gas would have a higher ϵ_{ff} (assuming the same free-fall time applies to the clouds in both cases). Any gas over the density threshold associated with the CN/HCN molecular lines may preferentially collapse to form stars. However, this is dependent on multiple layers of assumptions mentioned in Chapter 2. The conversion factors used in this thesis are assumed to be the same throughout all regions in a galaxy, and indeed throughout the entire sample. Though a relatively homogeneous sample of galaxies, applying such a sweeping generalization is less than ideal. Additionally, Bemis and Wilson (2023) suggest a dense gas fraction is likely reliable to trace gas over a certain constant density threshold (they suggest $10^{4.5}$ cm^{-3}), but is however not reliable for tracing gravitationally bound gas. The simplest models assume gravitationally bound clouds clump, collapse, and form stars (Usero et al. 2015).

Thus, gravitationally bound gas is what one might be interested in when studying star formation, rather than gas over an arbitrary density threshold.

Despite this, Figures 3.3 and 3.4 imply a continuous transition from the spiral data to that of the U/LIRGs in both bulk and dense molecular gas surface densities. This allows for some confidence in the gas surface density estimates. This also implies that in that parameter space, normal spirals and extreme galaxies alike all lie on the same distribution - albeit with spirals on the lower end of surface density. This continuity is not apparent in the SFR data, as there is an offset between the populations present in Figures 3.5 and 3.6. On the surface, this would suggest "external" factors play a big role driving star formation in addition to the gas content. Indeed, 13 galaxies in this sample are identified as merger galaxies (Stierwalt et al. 2013, Ledger et al. 2023), with Ledger et al. (2024, in prep) compiling them by merger stage. Highly active star formation in merger regions can aid in explaining significantly enhanced SFR in our sample; however there are other factors to consider. It is highly likely that the low end of the SFR data approaches the sensitivity limit of the data available. As mentioned in Chapter 2, only data above a noise threshold of 5σ is used for analysis. If the weakest radio continuum emission is indistinguishable from noise, it may be possible to draw incorrect conclusions regarding general trends in SFR. This is most notable in NGC 3256, which contains a prominent floor in Σ_{SFR}. As such, the star formation appears constant for this galaxy across a range of gas surface densities. Improved sensitivity could remove this floor, fill the gap between spiral and U/LIRG data, and adjust the fit presented in Figure 3.5. The shallow KS relationship found here creates some disagreement with other works that find extreme environments have stronger KS correlations (eg Wilson et al. 2019); more precise data may alleviate this. This offset in the data and the existence of a sensitivity floor can also be seen in the figures containing SFE.

There is some additional disagreement in the understanding of SFE and how it is predicted by surface densities. In examining the effects of the dense gas fraction (f_{dense}) on SFE_{dense}, Gao and Solomon (2004) found a flat relationship in multiple galaxy types (star forming spirals and LIRGS), implying a lack of correlation between those quantities. In contrast, newer findings potentially contain a negative correlation in normal star forming disks (Usero et al. 2015), Gallagher et al. 2018). This thesis itself examines the relationship in the sample of 16 U/LIRGs and finds only a weak negative correlation. This also enforces the notion that the dense gas fraction may not accurately trace gravitationally bound material by Bemis and Wilson (2023), and suggests that gas being over a certain density threshold does not necessarily cause it to initiate the star forming process.

The last relevant piece is that the tracer used in this thesis for dense gas was CN. This is important since this thesis uses a single conversion factor $I_{CN}/I_{HCN} = 0.86$ (the average from Wilson et al. 2023), even though the range of ratios goes from 0.76 to 1.10 (Wilson et al. 2023). It is likely that a prescription which uses a ratio on a galaxy-by-galaxy basis can lead to more accurate quantities for the dense gas fraction, the dense gas star formation correlation, and SFE_{dense}.

Chapter 4

Conclusion and Future Work

The goal of this thesis is to study and characterize the physics relating star formation and the gas content of some of the most extreme galactic environments. To achieve this, a sample of 16 luminous and ultra-luminous infrared galaxies is adopted from Ledger et al. (2023) in order to analyze quantities such as SFR, Σ_{mol} and Σ_{dense}, f_{dense}, SFE_{mol} and SFE_{dense}, and relationships between some of these quantities. These are all quantities that cannot be measured directly, and are instead estimated through tracers and conversion factors. Chapter 1 provides an overview of the literature on the relationship between star formation and gas in galactic environments, situating this thesis within the broader context of the field. Chapter 2 outlines the details of using radio continuum, CO (J=1-0), and CN (N=1-0) as tracers and the methods with which they are converted to physical quantities (SFR, Σ_{mol}, and Σ_{dense}). Additionally, it discusses the source of the data, and the use of CASA and the PHANGS-ALMA pipeline to process data from the ALMA telescope into science ready products. In Chapter 3, the findings and some interpretations are presented. The maps of SFE reveal that - in general - the peaks in free-free emission (the SFR tracer) correspond to peaks in SFE. This holds true for both SFE_{mol} and SFE_{dense}. In addition, the morphologies of the SFE_{mol} and SFE_{dense} maps generally agree with each other - although cases like NGC 3256 may be missing a peak in the SFE_{dense} map. The SFE_{dense} maps also systematically show a higher efficiency than SFE_{mol} - although what that means is a little nebulous on its own. Instead, the interpretation presented in Chapter 3 is to consider efficiency per free-fall time ($\epsilon_{ff} = \tau_{ff} \times SFE$), and ϵ_{ff} is higher for denser gas - potentially suggesting clouds above the "dense" threshold experience more efficient collapse to form stars.

In order to learn about the effect the gas content has on the SFR in the U/LIRG sample, Section 3.2 discusses various relationships between these quantities.

- The gas surface densities, both Σ_{mol} and Σ_{dense}, show a continuous transition between the spiral sample and U/LIRG sample. This also appears to be true for f_{dense}, which is not surprising given it is a ratio of the previous two quantities. Enhanced line emission is expected in U/LIRGs, but the f_{dense} is also higher. This can mean there is more gas over the 10^4 cm^{-3} threshold in U/LIRGs compared to spirals. It could also be that factors such as AGN enhance the HCN emission, causing it to trace gas under this density threshold.

- A Kennicutt-Schmidt scatter plot yielded a fit for the U/LIRGs which is shallower than the slope found in Wilson et al. (2019). The slope was nearly linear, and parallel to a fit for spirals - though with a significant offset to the fit from Lin et al. (2019). Two galaxies in particular may have pushed down the combined U/LIRG fit. NGC 3256 is likely at the sensitivity limit for radio continuum, leading to a floor in the data most easily seen in Figure 3.3. The other galaxy is

NGC 1068, which has bright free-free emission relative to its weaker line emission. A fit to the ULIRGs, a sub-sample which does not contain either of those galaxies, produces a much steeper fit closer to that of Wilson et al. (2019).

- A similar exercise pits Σ_{SFR} against the dense gas, Σ_{dense}. An offset between the spirals and U/LIRGs persists, though the correlation between Σ_{SFR} and Σ_{dense} appears tighter than the one to Σ_{mol}. This is consistent with the thinking of Gao and Solomon (2004), who suggested dense gas is more closely related to star formation than the bulk of gas.

- The SFE ends up having pronounced offsets which reflect the fact that the SFR is enhanced in the extreme environments in the U/LIRG sample. The U/LIRGs yield low depletion times (inverse of SFE_{mol}) around 10-100 Myr, with the spirals on the order of 0.3-3 Gyr. Other than SFE_{dense} being higher on average than SFE_{mol} (which is expected due to Σ_{dense} being smaller than Σ_{mol}), another key difference is that there is no correlation between SFE_{mol} and Σ_{mol}, whereas SFE_{dense} has a negative correlation with Σ_{dense}. A negative correlation also exists for SFE_{dense} and f_{dense}, which is contrary to the expected lack of correlation, or constant relationship (Gao and Solomon 2004).

There are some plans to take this work further. The first step is to consider the effects AGN have on the free-free and line emission, and exclude pixels near the AGN coordinates. Removing enhanced emission due to AGN contamination allows for greater confidence in the data, and could potentially alleviate the effects of potential outlier data such as some of the NGC 1068 pixels which may be affected by AGN (Ledger et al. 2023, Saito et al. 2022). Additionally, as of now this thesis only fits the

U/LIRG data. Especially in relationships between Σ_{mol} and Σ_{dense} or Σ_{mol} and f_{dense}, which have a continuous transition in the data, including the spiral data in the fit can add greater context. Another important adjustment can be made to assumptions such as the ratio CN/HCN. Currently this thesis adopts a constant ratio of 0.86, an average from Wilson et al. (2023). However, in that work the ratios have a range from 0.76 to 1.1 in the centre and 0.47 to 1.19 globally (Wilson et al. 2023), so applying the same ratio to all the galaxies in the sample would not be accurate. A paper from Bemis et al. (2024) is examining the use of a variable ratio and applying those techniques to this work may be appropriate and yield better estimates of Σ_{dense} and its related ratios.

This thesis has presented an analysis of the relationships between gas content and SFR for 12 LIRGs and 4 ULIRGs, resolved at 500 pc. This a relatively large and well-resolved sample of highly active galaxies which provide a crucial step into understanding the physics within these extreme environments. The continuation of this work will contribute to a deeper understanding of luminous and ultra-luminous infrared galaxies and their place within the broader context of star formation.

Appendix A

SFE maps

This appendix shows the SFE maps of the sample of galaxies in alpha-numerical order in Figures A1-A12. NGC 6240 and NGC 3256 are shown in Figures 3.1 and 3.2. NGC 3110 and NGC 5104 had no pixels in free-free emission above the 5σ noise cutoff, and are not included here.

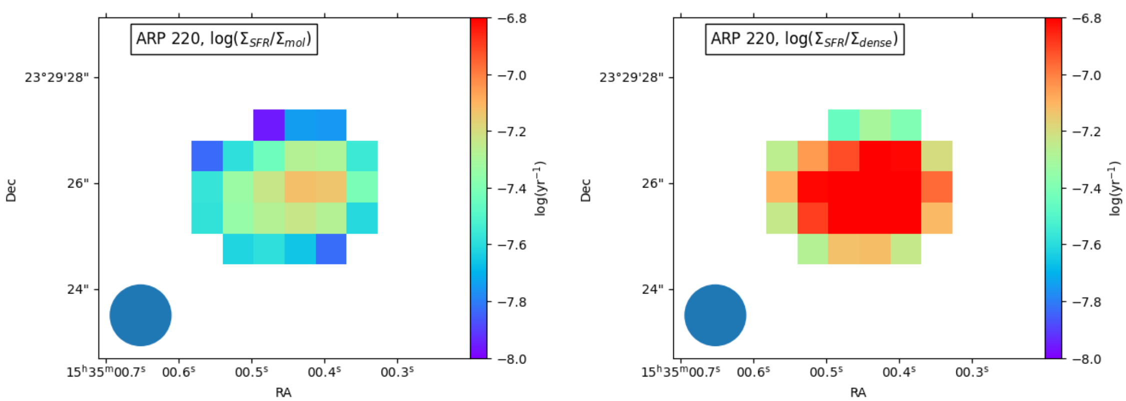

Figure A.1: (Left) SFE$_{mol}$ map for ARP 220. (Right) SFE$_{dense}$ map for that galaxy. The same field of view and beam are applied in both maps. The pixels in the SFE maps have noise cuts applied in molecular lines from Ledger et al. (2023) and a 5σ noise cut in radio continuum, and are the same as the pixels as the ones included in the scatter plots (e.g. Figure 3.5).

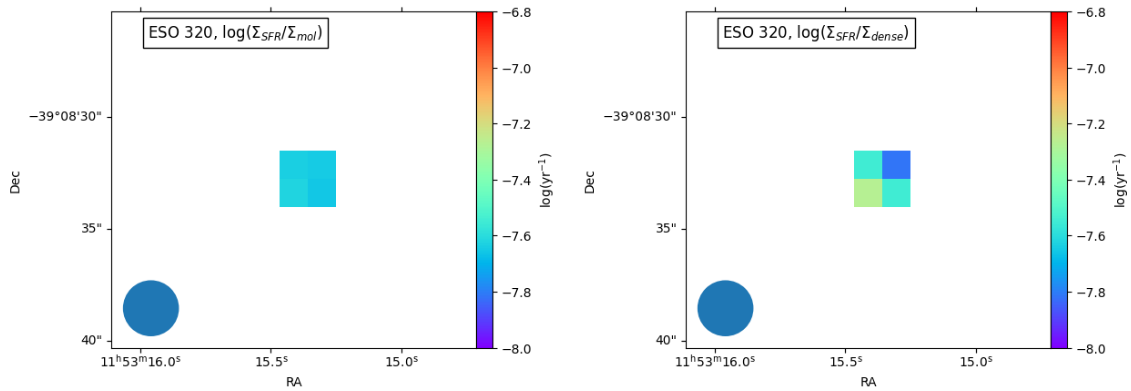

Figure A.2: (Left) SFE$_{mol}$ map for ESO 320. (Right) SFE$_{dense}$ map for that galaxy. See caption A.1 for details.

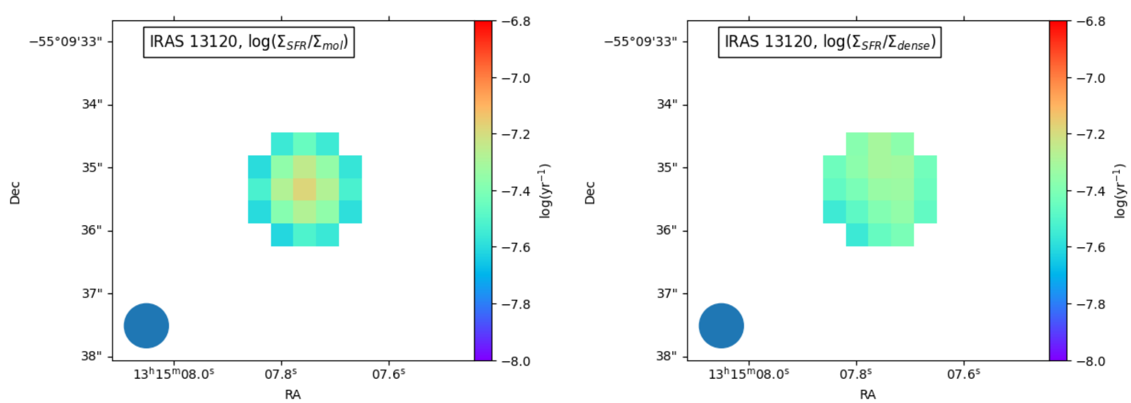

Figure A.3: (Left) SFE$_{mol}$ map for IRAS 13120. (Right) SFE$_{dense}$ map for that galaxy. See caption A.1 for details.

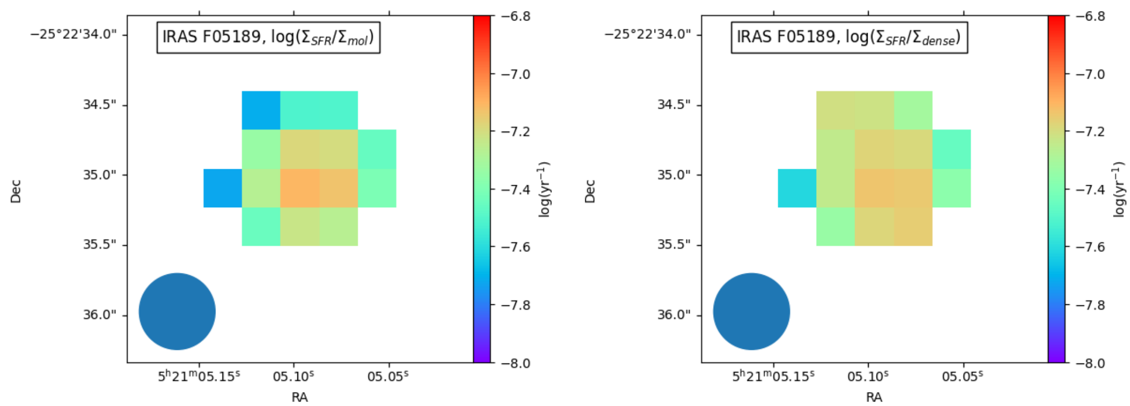

Figure A.4: (Left) SFE$_{mol}$ map for IRAS f05189. (Right) SFE$_{dense}$ map for the same galaxy. See caption A.1 for details.

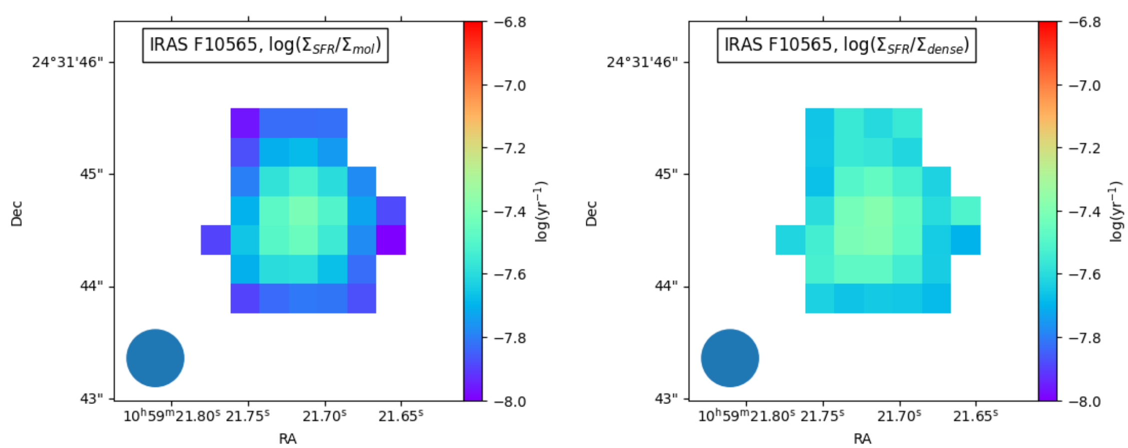

Figure A.5: (Left) SFE$_{mol}$ map for IRAS f10565. (Right) SFE$_{dense}$ map for the same galaxy. See caption A.1 for details.

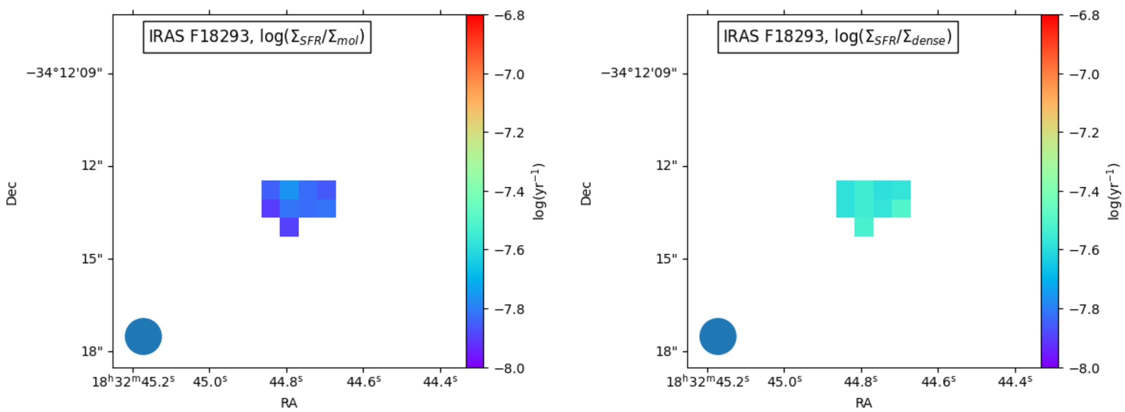

Figure A.6: (Left) SFE$_{mol}$ map for IRAS f18293. (Right) SFE$_{dense}$ map for the same galaxy. See caption A.1 for details.

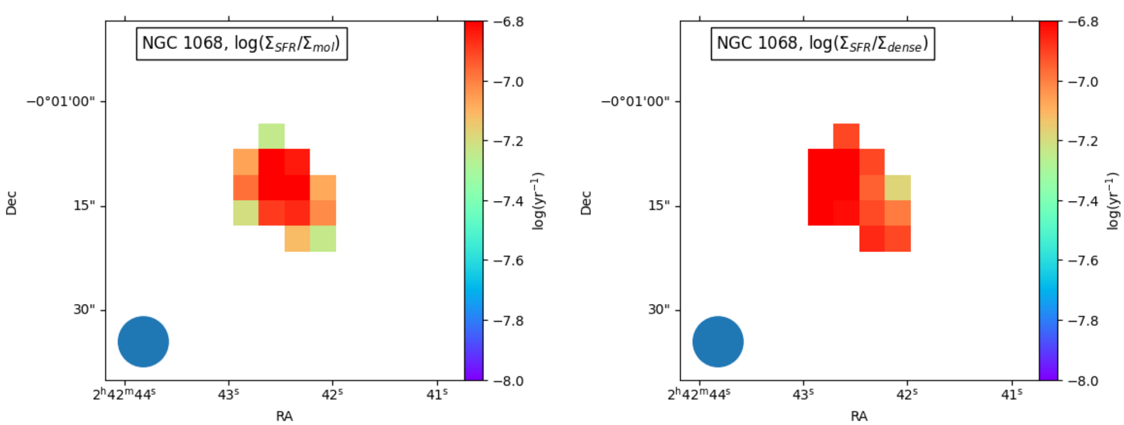

Figure A.7: (Left) SFE$_{mol}$ map for NGC 1068. (Right) SFE$_{dense}$ map for the same galaxy. See caption A.1 for details.

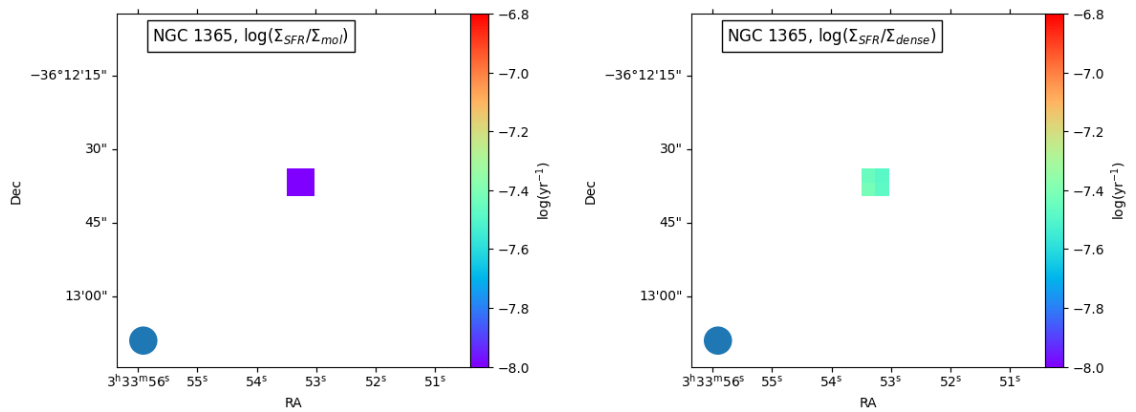

Figure A.8: (Left) SFE$_{mol}$ map for NGC 1365. (Right) SFE$_{dense}$ map for the same galaxy. See caption A.1 for details.

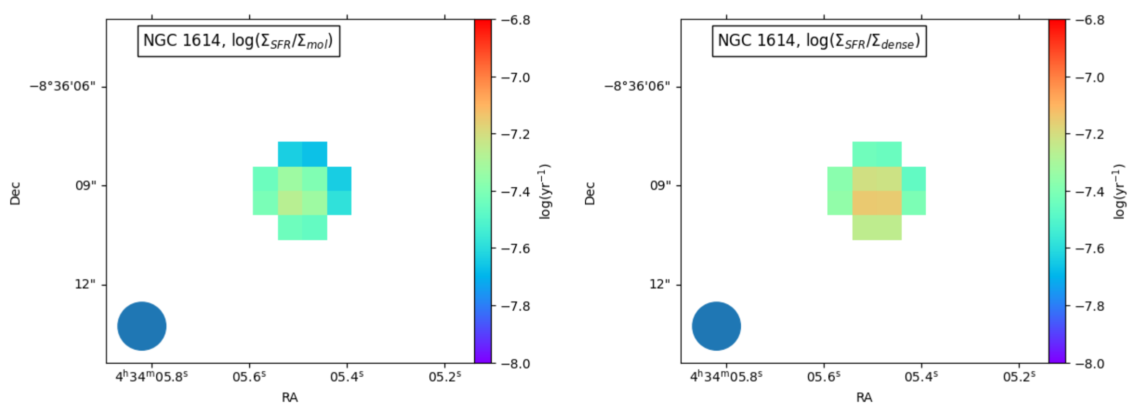

Figure A.9: (Left) SFE$_{mol}$ map for NGC 1614. (Right) SFE$_{dense}$ map for the same galaxy. See caption A.1 for details.

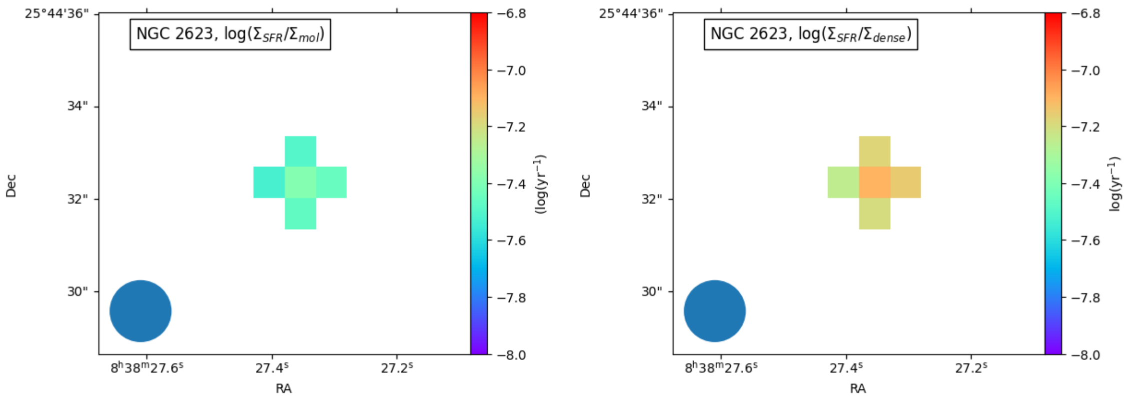

Figure A.10: (Left) SFE$_{mol}$ map for NGC 2623. (Right) SFE$_{dense}$ map for the same galaxy. See caption A.1 for details.

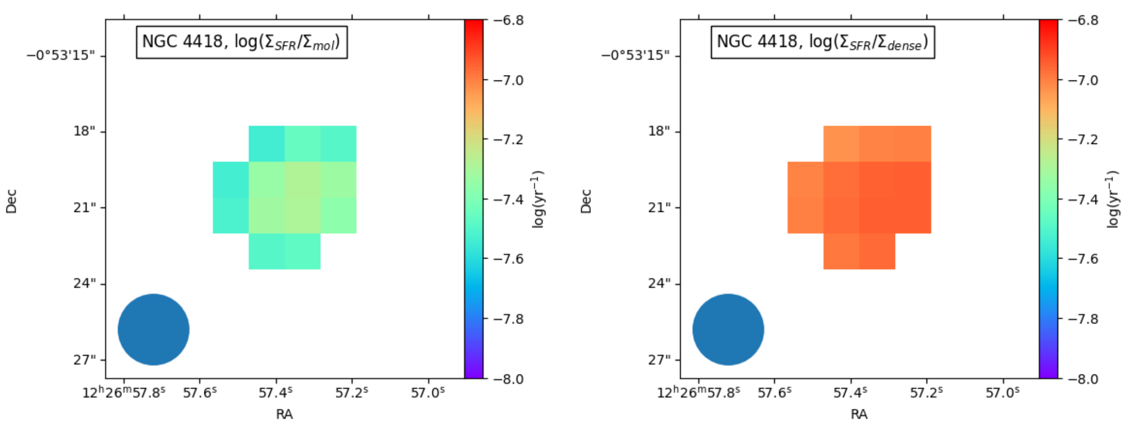

Figure A.11: (Left) SFE$_{mol}$ map for NGC 4418. (Right) SFE$_{dense}$ map for the same galaxy. See caption A.1 for details.

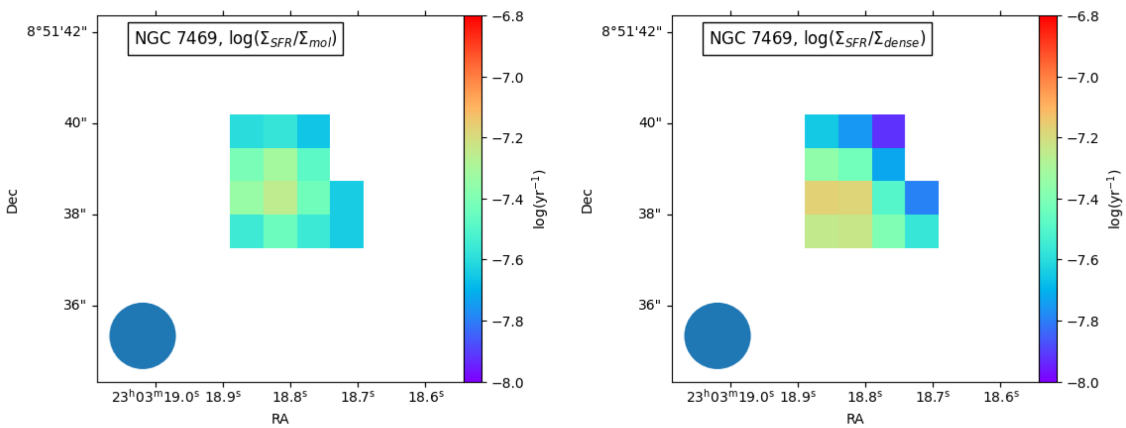

Figure A.12: (Left) SFE$_{mol}$ map for NGC 7469. (Right) SFE$_{dense}$ map for the same galaxy. See caption A.1 for details.

Bibliography

Armus, L. et al. (2009). GOALS: The Great Observatories All-Sky LIRG Survey. *Publications of the Astronomical Society of the Pacific*, 121(880):559.

Bemis, A. R. et al. (2024). submitted. *Astronomy and Astrophysics*.

Bemis, A. R. and Wilson, C. D. (2023). Does the HCN/CO Ratio Trace the Star-Forming Fraction of Gas? I. A Comparison with Analytical Models of Star Formation. *The Astrophysical Journal*, 945(1):42.

Bendo, G. J. et al. (2010). The Herschel Space Observatory View of Dust in M81. *Astronomy and Astrophysics*, 518(1):L65.

Bolatto, A. D. et al. (2013). The CO-to-H_2 Conversion Factor. *Annual Review of Astronomy and Astrophysics*, 51(1):207.

Buat, V. et al. (2010). Measures of Star Formation Rates from Infrared (Herschel) and UV (GALEX) Emissions of Galaxies in the HerMES Fields. *Monthly Notices of the Royal Astronomical Society: Letters*, Letters: 409(1):L1–6.

Collaboration, A. (2013). Astropy: A Community Python Package for Astronomy. *Astronomy and Astrophysics*, 558(A33):9.

Collaboration, A. (2018). The Astropy Project: Building an Open-science Project and Status of the v2.0 Core Package. *The Astronomical Journal*, 156(3):123.

Collaboration, A. (2022). The Astropy Project: Sustaining and Growing a Community-oriented Open-source Project and the Latest Major Release (v5.0) of the Core Package. *The Astrophysical Journal*, 935(2):167.

Downes, D. et al. (1993). Molecular Gas Mass and Far-Infrared Emission from Distant Luminous Galaxies. *The Astrophysical Journal Letters*, 414(1):L13.

Gallagher, M. J. et al. (2018). Dense Gas, Dynamical Equilibrium Pressure, and Star Formation in Nearby Star-Forming Galaxies. *The Astrophysical Journal*, 858:90.

Gallagher, M. J. et al. (2019). VizieR Online Data Catalog: Radial Profiles of 5 Nearby Galaxies (Gallagher+, 2018). *VizieR Online Data Catalog*, 185.

Gao, Y. and Solomon, P. M. (2004). The Star Formation Rate and Dense Molecular Gas in Galaxies. *The Astrophysical Journal*, 606(1):271.

García-Burillo, S. et al. (2012). Star-Formation Laws in Luminous Infrared Galaxies. New Observational Constraints on Models. *Astronomy and Astrophysics*, 539(A8).

Ginsburg, A. et al. (2019). radio-astro-tools/spectral-cube: Release v0.4.5. *https://zenodo.org/records/3558614*.

Harris, C. R. et al. (2020). Array Programming with NumPy. *Nature*, 585(7825):357.

Helou, G. (1986). The IRAS Colors of Normal Galaxies. *The Astrophysical Journal*, 311(1):L33.

Hirashita, H. et al. (2003). Star Formation Rate in Galaxies from UV, IR, and Hα Estimators. *Astronomy and Astrophysics*, 410(1):83.

Howell, J. H. et al. (2010). The Great Observatories All-Sky LIRG Survey: Comparison of Ultraviolet and Far-Infrared Properties. *The Astrophysical Journal*, 715(1):572–588.

Hunter, J. D. (2007). Matplotlib: A 2D Graphics Environment. *Computing in Science and Engineering*, 9(3):90.

Kelly, B. C. (2007). AGN-Driven Cold Gas Outflow of NGC 1068 Characterized by Dissociation-Sensitive Molecules. *The Astrophysical Journal*, 665(2):1489.

Kennicutt, R. C. (1989). The Star Formation Law in Galactic Disks. *The Astrophysical Journal*, 344(1):685.

Kennicutt, R. C. (1998). The Global Schmidt Law in Star-Forming Galaxies. *The Astrophysical Journal*, 498(2):541–552.

Kennicutt, R. C. and Evans, N. J. (2012). Star Formation in the Milky Way and Nearby Galaxies. *Annual Review of Astronomy and Astrophysics*, 50:531.

Kroupa, P. (1999). On the Variation of the Initial Mass Function. *Monthly Notices of the Royal Astronomical Society*, 322(2):231.

Ledger, B. et al. (2023). Stored in the Archives: Uncovering the CN/CO Intensity Ratio with ALMA in Nearby U/LIRGs. *Monthly Notices of the Royal Astronomical Society*, 527(2):2963–2990.

Ledger, B. et al. (2024). in prep. *Monthly Notices of the Royal Astronomical Society.*

Leitherer, C. et al. (1999). Starburst99: Synthesis Models for Galaxies with Active Star Formation. *The Astrophysical Journal Supplemet Series*, 123(1):3.

Leroy, A. K. et al. (2016). A Portrait of Cold Gas in Galaxies at 60 Pc Resolution and a Simple Method to Test Hypotheses That Link Small-Scale ISM Structure to Galaxy-Scale Processes. *The Astrophysical Journal*, 831(1):16.

Leroy, A. K. et al. (2021). PHANGS–ALMA Data Processing and Pipeline. *The Astrophysical Journal Supplement Series*, 255(1):19.

Li, Y. et al. (2010). TSpitzer 70 Mm Emission as a Star Formation Rate Indicator for Sub-Galactic Regions. *The Astrophysical Journal*, 725(1):677.

Lin, L. et al. (2019). The ALMaQUEST Survey: The Molecular Gas Main Sequence and the Origin of the Star-Forming Main Sequence. *The Astrophysical Journal Letters*, 884:L33(2).

McMullin, J. P. et al. (2007). CASA Architecture and Applications. *Astronomical Data Analysis Software and Systems XVI ASP Conference Series, Vol. 376, proceedings of the conference held 15-18 October 2006 in Tucson, Arizona, USA.*

Meyers, J. (2015). Jmeyers314/Linmix. *GitHub: https://github.com/jmeyers314/linmix*, page 155.

Murphy, E. J. et al. (2011). Calibrating Extinction-Free Star Formation Rate Diagnostics with 33 GHz Free-Free Emission in NGC 6946. *The Astrophysical Journal*, 737(2):67.

Pearson, C. et al. (2016). HERUS: A CO Atlas from SPIRE Spectroscopy of Local ULIRGs. *The Astrophysical Journal Supplement Series*, 227(1):9.

Persson, C. J. L. and Helou, G. (1987). On the Origin of the 40 - 120 Micron Emission of Galaxy Disks: A Comparison with Hα Fluxes. *The Astrophysical Journal*, 34(1):513.

Rosolowsky, E. and Leroy, A. K. (2006). Bias-Free Measurement of Giant Molecular Cloud Properties. *Publications of the Astronomical Society of the Pacific*, 118(842):590.

Saito, T. et al. (2022). AGN-Driven Cold Gas Outflow of NGC 1068 Characterized by Dissociation-Sensitive Molecules. *The Astrophysical Journal*, 935(2):155.

Sanders, D. B. and Mirabel, I. F. (1996). Luminous Infrared Galaxies. *Annual Review of Astronomy and Astrophysics*, 34:749.

Schmidt, M. (1959). The Rate of Star Formation. *The Astrophysical Journal*, 129(2):243.

Schruba, A. et al. (2011). A Molecular Star Formation Law in the Atomic-Gas-Dominated Regime in Nearby Galaxies. *The Astronomical Journal*, 142(2):37.

Solomon, P. M. and Bout, P. A. V. (2005). Molecular Gas at High Redshift. *Annual Review of Astronomy and Astrophysics*, 43(1):677.

Stierwalt, S. et al. (2013). Mid-Infrared Properties of Nearby Luminous Infrared Galaxies. I. Spitzer Infrared Spectrograph Spectra for the GOALS Sample. *The Astrophysical Journal Supplement Series*, 206(1):1.

Sun, J. et al. (2018). Cloud-Scale Molecular Gas Properties in 15 Nearby Galaxies. *The Astrophysical Journal*, 860(2):172.

Sun, J. et al. (2020). Molecular Gas Properties on Cloud Scales across the Local Star-Forming Galaxy Population. *The Astrophysical Journal*, 901(1):L8.

Usero, A. et al. (2015). Variations in the Star Formation Efficiency of the Dense Molecular Gas across the Disks of Star-Forming Galaxies. *The Astronomical Journal*, 150:115.

Virtanen, P. et al. (2020). SciPy 1.0: Fundamental Algorithms for Scientific Computing in Python. *Nature Methods*, 17(3):261.

Wilson, C. D. et al. (2019). The Kennicutt–Schmidt Law and Gas Scale Height in Luminous and Ultraluminous Infrared Galaxies. *The Astrophysical Journal*, 882(1):5.

Wilson, C. D. et al. (2023). A Nearly Constant CN/HCN Line Ratio in Nearby Galaxies: CN as a New Tracer of Dense Gas. *Monthly Notices of the Royal Astronomical Society*, 521(1):717–736.